Pergamon

Geochimica et Cosmochimica Acta, Vol. 67, No. 24, pp. 4705–4725, 2003

0016-7037/03 $30.00 + .00

doi:10.1016/S0016-7037(03)00463-0

Structural, chemical, and isotopic microanalytical investigations of graphite from supernovae

T. Kevin Croat,* Thomas Bernatowicz, Sachiko Amari, Scott Messenger, and Frank J. Stadermann
Department of Physics and McDonnell Center for the Space Sciences, Washington University, St. Louis, MO 63130, USA

(*Received February* 26, 2003; *accepted in revised form July* 3, 2003)

Abstract—We report the results of coordinated ion microprobe and transmission electron microscope (TEM) studies of presolar graphites from the KE3 separate (1.65–1.72 g/cm^3) of the Murchison CM2 meteorite. Isotopic analysis of individual graphites (1–12 μm) with the ion microprobe shows many to have large ^{18}O excesses combined with large silicon isotopic anomalies, indicative of a supernova (SN) origin. Transmission electron microscopy (TEM) of ultramicrotome slices of these SN graphites revealed a high abundance (25–2400 ppm) of internal titanium carbides (TiCs), with a single graphite in some cases containing hundreds of TiCs. Isotopic compositions of individual TiCs by nanoscale resolution secondary ion mass spectrometry (NanoSIMS) confirmed their presolar origin. In addition to TiCs, composite TiC/Fe grains (TiCs with attached iron–nickel subgrains) and solitary kamacite internal grains were found. In the composite grains, the attached iron phase (kamacite [0–24 at. % Ni] or taenite [up to 60 at. % Ni]) was epitaxially grown onto one or more TiC faces. In contrast to the denser Murchison KFC1 graphites, no Zr-Ti-Mo carbides were observed. The average TiC diameters were quite variable among the SN graphites, from 30 to 232 nm, and were generally independent of the host graphite size. TiC grain morphologies ranged from euhedral to anhedral, with the grain surfaces exhibiting variable degrees of corrosion, and sometimes partially amorphous rims (3 to 15 nm thick). Partially amorphous rims of similar thickness were also observed on some solitary kamacite grains. We speculate that the rims on the internal grains are most plausibly the result of atom bombardment caused by drift of grains with respect to the ambient gas, requiring relative outflow speeds ~100 km/s (i.e., a few percent of the SN mass outflow speed).

Energy dispersive X-ray spectrometry (EDXS) of TiCs revealed significant V in solid solution, with an average V/Ti ratio over all TiCs of ~83% of the solar value of 0.122. Significant variations about the mean V/Ti ratio were also seen among TiCs in the same graphite, likely indicating chemical equilibration with the surrounding gas over a range of temperatures. In general, the diversity in internal TiC properties suggests that TiCs formed first and had substantially diverse histories before incorporation into the graphite, implying some degree of turbulent mixing in the SN outflows.

In most graphites, there is a decrease in the number density of TiCs as a function of increasing radial distance, caused by either preferential depletion of TiCs from the gas or an acceleration of graphite growth with decreasing ambient temperature. In several graphites, TiCs showed a trend of larger V/Ti ratios with increasing distance from the graphite center, an indication of progressive equilibration with the surrounding gas before they were sequestered in the graphites. In all but one graphite, no trend was seen in the TiC size vs. distance from the graphite center, implying that appreciable TiC growth had effectively stopped before the graphites formed, or else that graphite growth was rapid compared to TiC growth. Taken together, the chemical variations among internal grains as well as the presence of partially amorphous rims and epitaxial Fe phases on some TiCs clearly indicate that the phase condensation sequence was TiC, followed by the iron phases (only found in some graphites) and finally graphite. Since graphite typically condenses at a higher temperature than iron at low pressures ($<10^{-3}$ bars) in a gas with C > O and otherwise solar composition, the observed condensation sequence implies a relative iron enrichment in the gas or greater supersaturation of graphite relative to iron.

The TEM observations allow inferences to be made about the physical conditions in the gas from which the grains condensed. Given the TiC sizes and abundances, the gas was evidently quite dusty. From the observed TiC size range of ~20 nm to ~500 nm (assuming ~1 yr growth time and T ~ 1800°K), we infer minimum Ti number densities in the gas to be ~7×10^4 to ~2×10^6 atoms/cc, respectively. Although the gas composition is clearly not solar, for scale, these number densities would correspond to a pressure range of ~0.2 μbar to ~5.0 μbar in a gas of solar composition. They also correspond to minimum TiC grain number densities of ~3×10^{-4} to ~0.2 grains/cc, assuming complete condensation of Ti in TiC. We estimate the maximum ratio of mean TiC grain separation distance in the gas to grain diameter from the Ti number densities as ~3×10^5 to ~1×10^6.

Now it is the microscopic which is the profound reality, for it underlies the macroscopic; it is in it that it is necessary to seek the ultimate mysteries of reality which, in the macroscopic, conceal themselves under the lack of precision of the sensory data and in the confused mass of statistical averages.

Louis De Broglie
Physics and Microphysics (1955)

1. INTRODUCTION

Presolar grains are minerals found in primitive meteorites that were present in the protosolar nebula, having formed

* Author to whom correspondence should be addressed (tkc@wuphys.wustl.edu).

previously in the mass outflows from red giant stars, novae, and supernovae. They are identified as such on the basis of clearly nonsolar isotopic compositions in major or minor elements that could not have resulted from nuclear-specific processes since the formation of the solar system. Isotopic studies of presolar grains, coupled with theoretical models and astronomical observation, provide clues to the specific classes of stellar objects from which the grains originated, and give detailed information on stellar nucleosynthesis (see reviews by Bernatowicz and Walker, 1997; Bernatowicz and Zinner, 1997; Zinner, 1998). Mineralogical and microstructural studies of presolar grains (e.g., Bernatowicz et al., 1991, 1996; Bernatowicz and Cowsik, 1997; Daulton et al., 2002, 2003) also have provided insights into grain formation in circumstellar outflows, at a level of detail far beyond that previously attainable from remote astronomical observations. The growing list of presolar materials discovered in meteorites includes silicon carbide, nanodiamonds, silicon nitride, various magnesium, titanium, and aluminum oxides, and graphite (Zinner, 1998), as well as refractory Ti, V, Fe, Zr, Mo, Ru carbides and FeNi metals present as subgrains within presolar graphite (Bernatowicz et al., 1996; Croat et al., 2002).

In the present work we discuss the results of coordinated ion microprobe and transmission electron microscope (TEM) studies on a subset of individual presolar graphites from the Murchison CM2 meteorite (Amari et al., 1995), inferred from their isotopic compositions to have originated in the outflows of supernovae (SN). Several nuclides serve as diagnostic indicators of a SN environment of grain condensation. The isotopic composition of the major element carbon itself is not diagnostic of a SN origin, because He burning (producing ^{12}C) and the CNO cycle (producing ^{13}C) are operative in all stellar sources, whether or not they evolve into SN. Therefore, to deduce a SN origin, one must rely on the isotopic composition of minor elements that are either present in subgrains of other minerals within the graphite, or else were trapped within the graphite itself during its formation. Radioactive ^{44}Ti ($T_{1/2}$ = 60 a) is only produced by explosive nucleosynthesis at high temperatures deep within SN, and its initial presence at the time of grain condensation can be detected as an enrichment in its daughter ^{44}Ca, as originally predicted by Clayton (1975). Similarly, large inferred excesses of ^{41}K from ^{41}Ca ($T_{1/2} = 1.03 \times 10^5$ a) and ^{26}Mg from ^{26}Al ($T_{1/2} = 7.4 \times 10^5$ a) are fairly diagnostic of SN, provided that they far exceed what is expected to be produced in other stellar sources (Amari and Zinner, 1997). Large excesses of stable ^{28}Si are produced only by SN and can establish presolar grains as SN condensates. Excesses of the other two stable Si isotopes, ^{29}Si and ^{30}Si, are also produced by neutron reactions in the He-burning shell of asymptotic giant branch (AGB) stars, but very large excesses of these isotopes are produced only in SN. Finally, large excesses of ^{18}O originate deep within all massive stars, including Wolf-Rayet stars and SN, but a SN origin is indicated when these excesses are accompanied by large ^{28}Si excesses (Travaglio et al., 1999).

In addition to giving detailed insights into explosive nucleosynthesis, the study of presolar SN grains can provide otherwise unattainable information on the products and mechanisms of grain formation in SN outflows. In traditional astronomical studies, infrared (IR) spectroscopy has been used successfully to identify mineral phases in dust surrounding various types of stars. For example, features of both silicates (Woolf and Ney, 1969) and SiC (Treffers and Cohen, 1974; Merrill and Stein, 1976; Cohen, 1984) have been found around AGB stars. Excess emission in the IR has been observed in many SN and is interpreted as originating from heated dust (Gilra and Code, 1971; Woolf, 1973). But although dust condensation around SN has been unambiguously observed (Meikle et al., 1993; Roche et al., 1993; Wooden et al., 1993; McCray, 1993), only limited inferences can be drawn regarding the nature of the dust from the astronomical observations. Silicate formation has been inferred in various spectra from SN remnants (Arendt et al., 1999). Unfortunately, SN 1987A, which provided the best evidence for dust condensation in core-collapse SN, had a featureless spectrum with no evidence of silicate or SiC formation. This spectrum is consistent with the condensation of graphite or iron grains, or both (Wooden, 1997), but such identifications are somewhat speculative as the IR features of these minerals are not sufficiently distinct. In general, IR astronomy can conclusively determine when and where dust has formed around a SN, but is very limited in its ability to characterize SN dust further in terms of its mineralogy, chemical composition, or size. Given these limitations, the isotopic, chemical, and mineralogical studies of SN presolar dust grains in the laboratory promise to provide more detailed information that can advance our understanding of grain formation in the supernova outflows.

Earlier TEM studies (Bernatowicz et al., 1996) of presolar graphite spherules from the Murchison KFC1 graphite separate (mean diameter = 2 μm; 2.15–2.20 g/cc; Amari et al., 1994) revealed the presence of internal grains in some graphites, mostly refractory carbides (Ti, Zr, Mo, and Ru carbides and their solid solutions). Bernatowicz et al. (1996) concluded that the condensation of Zr-Ti-Mo carbides before graphite requires an s-process enrichment of Zr and Mo to at least 30 times their solar proportions. The most plausible stellar sources of the graphites containing such carbides are low mass (1–3 mol/L_{Sun}) N-type carbon stars, which typically have s-process enrichments of heavy elements (e.g., Zr, Ba, and rare earth elements) that are 10–100 times their solar proportions (Lodders and Fegley, 1995, 1997). The TEM observations were used therefore in conjunction with detailed equilibrium condensation calculations for a gas of solar composition (except for enhanced C/O and s-process elements; Lodders and Fegley, 1995; Sharp and Wasserburg, 1995) to infer the pressures, C/O ratios, and temperatures during grain formation. However, due to the small size of the graphites and the degree of grain ablation during ion microprobe analyses, both TEM and isotopic studies could not be done on the same spherule. Instead, suites of grains were studied by each technique separately, but the results could not be directly correlated. Later correlated isotopic and TEM studies of larger (4–12 μm) graphites from Murchison, which did show the isotopic signatures of SN, revealed many internal titanium carbides (TiCs) (Bernatowicz et al., 1998; Bernatowicz et al., 1999; Croat et al., 2002) as well as several FeNi metal grains (kamacite). From the observed microstructure in these SN graphites, it was concluded that TiC condensed first and then was incorporated into growing graphite spherules. However, the formation sequence of several condensates is not sufficient information for equilibrium thermodynamic modeling of condensation in the SN outflow, be-

cause a solar-like gas composition cannot be assumed. The situation is complicated further by turbulent mixing of the various SN shells in the outflowing material, as inferred from astronomical observation (Wooden, 1997), from hydrodynamic modeling (Herant and Woosley, 1994), and from the isotopic compositions of SN grains themselves (Amari and Zinner, 1997).

This study focuses on low-density graphite spherules from density separate KE3 (1.65–1.72 g cm^{-3}) of the Murchison meteorite. The spherules studied were selected on the basis of isotopic compositions determined by ion microprobe analyses, in particular large excesses in ^{18}O and large variations in the Si isotopes (typically ^{28}Si excesses) indicative of a supernova origin (Amari et al., 1995). As in the previous TEM studies of graphites, abundant internal titanium carbide crystals (TiCs) were found (25–2400 ppm by volume)—in several graphites literally hundreds of them. The abundance of internal TiCs permitted the collection of aggregate data on the internal refractory grain populations, such as the grain size distribution, major element ratios, trace element abundances, degree of corrosion, and spatial distribution. Trends in these properties as a function of radial position, which is correlated with graphite growth time, were also investigated. In addition, FeNi subgrains were found epitaxially grown onto the surfaces of some TiCs (within a subset of the SN graphites). These composite grains yield further detailed information about the condensation sequence. Along with the TEM analyses and conventional ion microprobe characterization of the bulk isotopic composition of the graphites, the distribution of isotopes within some of the graphites and among their larger internal grains were mapped isotopically using nanoscale resolution secondary ion mass spectrometry (NanoSIMS) (Stadermann et al., 2003). Together, the detailed chemical, structural, and isotopic microanalytical data on the individual graphites and their internal grains provide a wealth of information with which to decipher the formation history of SN graphites.

2. MATERIAL AND METHODS

2.1. Isotopic Characterization

Graphites were obtained from the KE3 density separate (1.65–1.72 g cm^{-3}) of the Murchison meteorite, a subfraction of KE1 (Amari et al., 1994). The grains were dispersed on gold foil-covered scanning electron microscope (SEM) mounts and imaged in a JEOL 840A SEM to locate large spherical graphites (1–12 μm), a type of grain morphology tending to indicate a presolar origin (Hoppe et al., 1995). These large graphites were then isotopically characterized with a Cameca IMS 3f ion microprobe for C, O, and Si, and for other trace elements when these were sufficiently abundant (N, Mg, Al, Ca, Ti, and Cr). Details of the isotopic measurement method have been described previously (Zinner et al., 1989; Hoppe et al., 1995).

2.2. TEM Sample Preparation and Characterization

After isotopic characterization, graphite grains with large anomalous isotopic compositions (especially low $^{16}O/^{18}O$ ratios and large Si isotope anomalies) and of sufficient size (4–10 μm) were prepared for TEM study. A selected graphite was first picked from the ion probe mount using a sharpened tungsten needle ($\approx$1 μm diameter at the tip) held in a micromanipulator. The tungsten needles were electrochemically cleaned and sharpened frequently in sodium hydroxide solution. During the process, the graphite was viewed with a Nikon Eclipse E600 microscope (1.4 cm working distance, 1000$\times$ typical magnification). Using the micromanipulator, each graphite was placed at the bottom of a gelatin capsule, along with several small carbon fibers to aid in later locating the graphite. A nearby americium source was used to minimize charging problems, which can prevent grains from properly detaching from the tungsten needle. The gelatin capsule was slowly filled with resin (LR White Hard) using a 29-gauge syringe, and then cured at 60°C for a day. The gelatin capsule was then removed, leaving a resin block containing the grain and the carbon fibers at its tip. The tip of this resin block was trimmed into a square plateau 250 μm on a side, and then sliced with an ultramicrotome (Reichert-Jung Ultracut E) equipped with a diamond knife attached to a water reservoir. The 70-nm-thick slices of the graphite grains and their surrounding resin were then removed from the water surface onto 3-mm, 75-mesh holey-carbon-coated Cu TEM grids. Due to sample ablation during the preliminary isotopic analysis, and because only $\sim$50% of the TEM grid consists of open area, the effective volume of any graphite spherule available for TEM analysis is generally $\sim$1/3 of the original spherule volume.

The morphology and chemical composition of the graphite and its internal grains were determined with a JEOL 2000FX TEM equipped with a NORAN Vantage energy-dispersive X-ray spectrometer (EDXS). For the present study, locating internal crystals trapped within the graphite was of primary interest, for which an accurate and efficient method was needed. In general, internal crystals are not visible in image contrast unless the angle between a crystal plane and the electron beam satisfies the Bragg diffraction condition. Thus, to detect internal crystals, all graphite slices were observed at high magnification ($\sim 10^5$ $\times$) while the sample stage was systematically tilted through a 30°-45° range about one goniometer axis. Once located, crystals could be rotated about the two axes of the sample stage goniometer using Kikuchi bands to identify the major crystallographic zones (<001>, <011>, and <111> of cubic crystals), which also yield the maximum contrast with respect to the background graphite. Using this method, internal grains as small as 10 nm were detected, although the estimated limit of likely detection is slightly lower ($\approx$5 nm). The probability of detecting smaller crystals decreases due to the lower diffracted electron intensities and due to the fact that such small grains can be masked by the prevalent contrast features in this size range (<5 nm), which are {002} reflections from the graphite. However, it is quite unlikely that numerous TiC grains exist in this size range, because the composition of many such contrast features was measured with EDXS and showed no Ti.

Multiple selected area diffraction (SAD) or microdiffraction patterns of high symmetry zones, or both, were used for conclusive phase identification, along with EDXS chemical composition information. For unknown phases, a complete set of low-index zone axis patterns (typically 3–4) were analyzed by digitization of diffraction negatives. The diffraction rings from the in-plane {100} and {110} graphite reflections also present in the SAD patterns were used for internal calibration of d-spacings as well as to correct for astigmatism. Using this method, the unit cell parameters for TiC were determined to better than 1% as 4.39 $\pm$ 0.03, $\sim$1.5% larger than the reported values for synthetic TiC (4.327Å fcc) and terrestrial TiC (khamrabaevite, 4.319Å fcc, 46% Ti, 25% V, 9% Fe, 20% C by weight; Roberts et al., 1990). Several iron–nickel phases, namely kamacite (bcc, a $\approx$ 2.97Å) and taenite (fcc, a $\approx$ 3.65Å) were similarly identified. Due to their widespread presence, many TiCs were identified on the basis of their chemical composition along with a single diffraction pattern of a low index zone axis. More extensive diffraction data, both SAD and microdiffraction patterns, were required for the characterization of composite (TiC/Fe) grains having a FeNi phase epitaxially grown onto TiC. The epitaxial nature of this growth was demonstrated (as discussed below) by finding the orientation relationship from diffraction patterns, which showed alignment of low-index crystallographic zones of both crystals. SAD patterns allowed accurate measurement of the mismatch and misorientation of the crystals, whereas microdiffraction patterns taken from smaller areas made identification of the crystal structures of submicron grains easier. Due to the tilt limitations of the TEM stage, the orientation relationship could only be determined for some of the TiC/Fe grains (typically when the interface plane between the phases was approximately parallel to the TEM beam).

EDXS spectra were first used to identify the elements present, with careful attention paid to the possibility of artifact peaks or shifts in the energy calibration. The Norvar window of the EDXS system allowed measurement of all elements with $Z \geq 5$. After qualitative examination, quantitative analysis was performed using our own software scripts (executed within the Microcal Origin software package). The intensity

Table 1. Bulk isotopic data for KE3 graphites studied in the TEM[a].

Graphite #	Diameter (μm)	$^{12}C/^{13}C$	$^{16}O/^{18}O$	$\delta^{29}Si$ (per mil)[b]	$\delta^{30}Si$ (per mil)[b]
d7	6.3	107.1 ± 0.4	49 ± 1	−325 ± 53	−539 ± 42
e7	5.7	92.2 ± 0.6	100 ± 3	−227 ± 47	−290 ± 45
e10	12.0	125.2 ± 0.7	174 ± 7	−85 ± 31	−123 ± 30
e15	5.1	59.7 ± 0.3	236 ± 9	11 ± 63	−93 ± 59
f331	6.8	190.0 ± 1.3	202 ± 2.6	412 ± 62	369 ± 59
f542	5.3	1580 ± 17.5	351 ± 16	−139 ± 26	−92 ± 38
e3	5.9	282.0 ± 2.6	298 ± 11	−52 ± 28	−43 ± 29
e6	6.8	231 ± 2	290 ± 12	−1 ± 32	−11 ± 32
e11	5.9	81.5 ± 0.4	320 ± 10	−66 ± 29	−79 ± 29
f131	5.9	110.0 ± 0.32	84 ± 18	−279 ± 48	−317 ± 29
e4	10.2	8.9 ± 0.2	536 ± 34	49 ± 74	46 ± 74
e8	4.4	10.79 ± 0.02	514 ± 27	−122 ± 55	−217 ± 52

[a] Grouped according to types of internal grains present (see Table 2).
[b] $\delta^{x}Si = 1000[(^{x}Si/^{28}Si)_{sample}/(^{x}Si/^{28}Si)_{Solar} - 1]$

from each element was determined by integration over the characteristic peak using a window of 1.2 full width half-maximum. The background intensity was subtracted from this value, using two identical windows above and below the characteristic peak, a method accurate for peaks above 1.5 keV (true for all peaks except C and O, which could not be accurately quantified; Williams and Carter, 1996). The carbon content of internal grains could not be determined accurately because a significant number of counts from the graphite were always measured. The background-subtracted counts were then corrected with k-factors, as determined from geologic standards (chromite USNM 117075, ilmenite USNM 96189). A well-characterized standard for V was unavailable, so standard values of the relative correction factor for a 200-keV TEM were used (Sheridan, 1989). The V-K_α counts are effectively increased by 1.03 ± 0.01 relative to the Ti-K_α counts. The uncertainty in this k-factor is a negligible source of error in the calculated V/Ti atomic ratios. A pathologic overlap of the Ti-K_β and V-K_α peaks occurs in the typical TiC spectra, complicating V quantization. To correct for this overlap, the ratio of Ti-K_α/Ti-K_β was accurately measured in a Ti elemental standard (Ti-K_β/Ti-K_α = 0.13 ± 0.01). From this ratio and the Ti-$K_\alpha$magnitude, the number of counts from Ti-K_β was determined and subtracted from the V-K_α channel. This quantitative analysis method was carefully tested and gave self-consistent results when applied to multiple spectra from the same grain. It was also compared with the quantitative results from the NORAN Vantage software, and was found to give more consistent results. Errors (2σ) reported here for EDXS measurements were determined from Poisson counting statistics.

To compare the various SN graphites, the overall abundance of TiCs and their distance from the center of the graphite spherule were also determined. The abundance of internal crystals (TiCs) was determined from the fractional cross-section area of the TiCs relative to the graphite. For thin samples, this areal fraction approximately equals the volume fraction (Delesse relation). The internal TiCs were modeled as ellipsoids in projection, and their areas were determined by major and minor axis measurements made directly from TEM images. The graphite area was determined from direct pixel counting of thresholded TEM images using NIH ImageJ software. This method was necessary to prevent holes in the graphite from artificially inflating the TiC areal fraction. The radial distance of individual internal grains from the center of the graphite spherule was calculated using 1) the distance of a grain from the center of the slice in which it was found and 2) the distance of a particular slice from the center of the graphite spherule as inferred from the slice diameter.

2.3. Nano SIMS Analysis

After analytical TEM characterization, selected TEM grids were mounted on a conducting substrate and analyzed in the CAMECA NanoSIMS to obtain the isotopic composition of C, N, O, and sometimes Ti. Bulk isotopic measurements of the graphite in the NanoSIMS were found to be consistent with bulk measurements in the IMS 3f ion microprobe. The isotopic compositions of internal TiC grains were also measured, revealing significant isotopic anomalies and thus providing direct proof of their presolar origin. Details of the measurement techniques and results for these KE3 graphite spherules are given by Stadermann et al. (2003).

3. RESULTS

3.1. Bulk Isotopic Composition of Low-density Graphites

Most of the spherical graphites in the KE3 fraction of the Murchison meteorite (Amari et al., 1995) were determined to be of presolar origin on the basis of isotopic composition, with only ~10% having solar isotopic ratios in C (solar $^{12}C/^{13}C$ = 89.9), O (solar $^{16}O/^{18}O$ = 499), and Si (solar $^{29}Si/^{28}Si$ = 0.0506; $^{30}Si/^{28}Si$ = 0.0334) within analytical uncertainty (solar ratios from Anders and Grevesse, 1989). The percentages of graphites with significant ($>2\sigma$) isotopic deviations from solar ratios were 88%, 63%, and 40% for carbon, oxygen, and silicon, respectively. To understand why these percentages are lower for the trace elements O and Si than for the major element C, it is important to note that O and Si are only accidentally included in the graphite during its growth. Thus, if these elements are present in only very low amounts in a given graphite (~1 wt.%; Hoppe et al., 1995), not only are the fractional analytical uncertainties much greater than for C, but contributions from terrestrial sources (e.g., from the sample mount) can become significant and dominate the isotopic composition. In the present work, 10 graphites with large isotopic excesses in ^{18}O were selected for TEM study (Table 1). Of these, two (e6 and e15) have Si isotopic compositions indistinguishable from solar, and so a massive (non-SN) star origin cannot strictly be ruled out. In addition, two other graphites (e4 and e8) of unknown origin with normal oxygen isotopic ratios within error but very low $^{12}C/^{13}C$ ratios were selected for comparison. One of these (e8) has a ^{28}Si excess typical of SN graphites, but the other (e4) has no ^{28}Si excess, so we cannot confidently ascribe its origin to a SN.

The bulk isotopic data (± 1σ analytical uncertainty) and spherule diameters determined from SEM images for the 12 KE3 graphites studied in the TEM are presented in Table 1. The isotopic data are also displayed in Figure 1 [separate two-

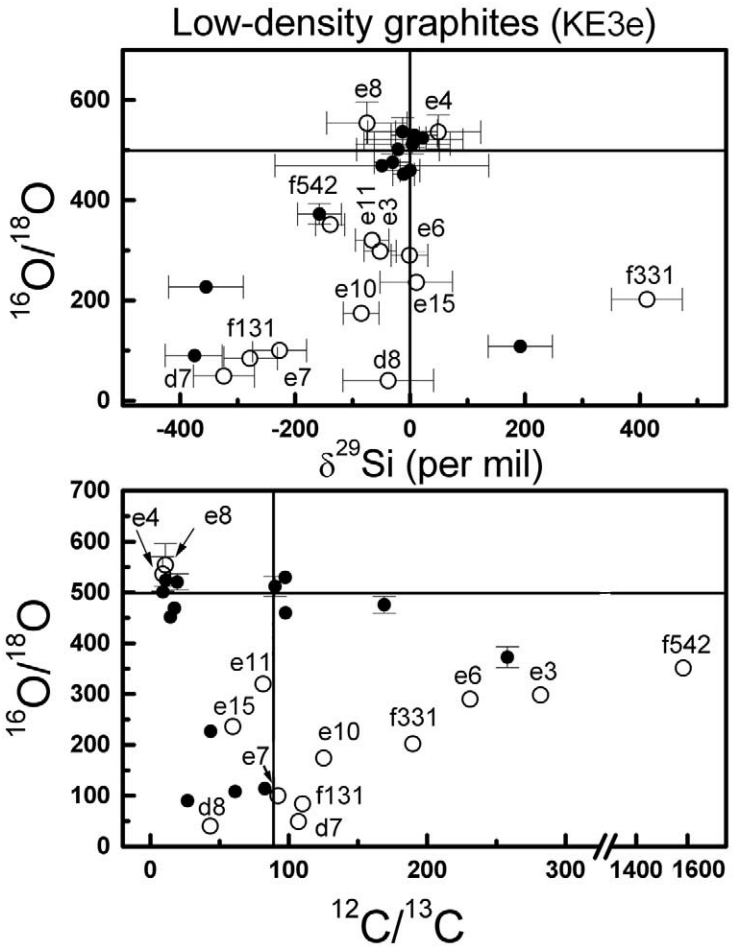

Fig. 1. Bulk isotopic data for spherical KE3 graphites (reproduced from Travaglio et al., 1999), presented as separate two-isotope plots of the $^{16}O/^{18}O$ isotopic ratio vs. $\delta^{29}Si$ (per mil deviation from solar value) and the $^{12}C/^{13}C$ isotopic ratio. Graphites also studied in the TEM are indicated by open symbols and are labeled. The solid lines indicate the solar isotopic ratios.

isotope plots showing $^{16}O/^{18}O$ vs. $\delta^{29}Si$ and $^{16}O/^{18}O$ vs. $^{12}C/^{13}C$; d8 previously studied by Bernatowicz et al. (1999) are included in Fig. 1 but not in Table 1] along with data for other KE3 graphites (Travaglio et al., 1999) that were mostly consumed by the ion probe measurements, thereby leaving insufficient material for TEM study.

3.2. Structure and Chemical Composition of KE3 Graphites

Presolar graphites show varying degrees of graphitization, a phenomenon also seen in terrestrial carbonaceous material (Buseck and Huang, 1985). At opposite extremes are the so-called "onion" and "cauliflower" types of presolar graphite (Bernatowicz et al., 1991, 1996). The onion type consists of long-range concentric layers of well-graphitized carbon, with interlayer d-spacings no more than 5% larger than for perfect graphite (0.3355 nm). This graphite often encloses a core of nanocrystalline carbon consisting of up to 3–4 nm diameter graphene sheets (planar networks of aromatic hexagonal rings) with no evidence of stacking order in the third dimension (Bernatowicz et al., 1996). These cores show electron diffraction rings from the graphene sheets ({*h*00} and {*hk*0}), but no reflections from {00*l*} planes. The cauliflower type consists of short, curved and discontinuous platelets of turbostratic graphite arranged concentrically, like a ball of scales, without long-range continuity in the stacking layers, and showing {*h*00} and {*hk*0} electron diffraction rings along with reflections from the {00*l*} planes (Bernatowicz et al., 1991, 1996). In this study, TEM examinations of cross-sections from the spherical graphites showed concentric turbostratic layers (Fig. 2) with a degree of graphitization intermediate between the onion and cauliflower types. Wide-area SAD patterns showed the {*h*00} and {*hk*0} rings from the graphene sheets, along with {00*l*} reflections from the stacking of these sheets. The average c-axis unit cell dimension was determined to be 7.3 ± 0.1 Å, which is 8% larger than the c-dimension from well-ordered graphite (hexagonal, a = 2.46Å, c = 6.70Å). EDXS of the graphite itself (away from any internal grains) revealed mainly carbon, along with trace amounts of Si and sometimes O, Fe, and Ca. These other elements appeared to be uniformly distributed within the graphite, apparently accidentally trapped within the layers, and

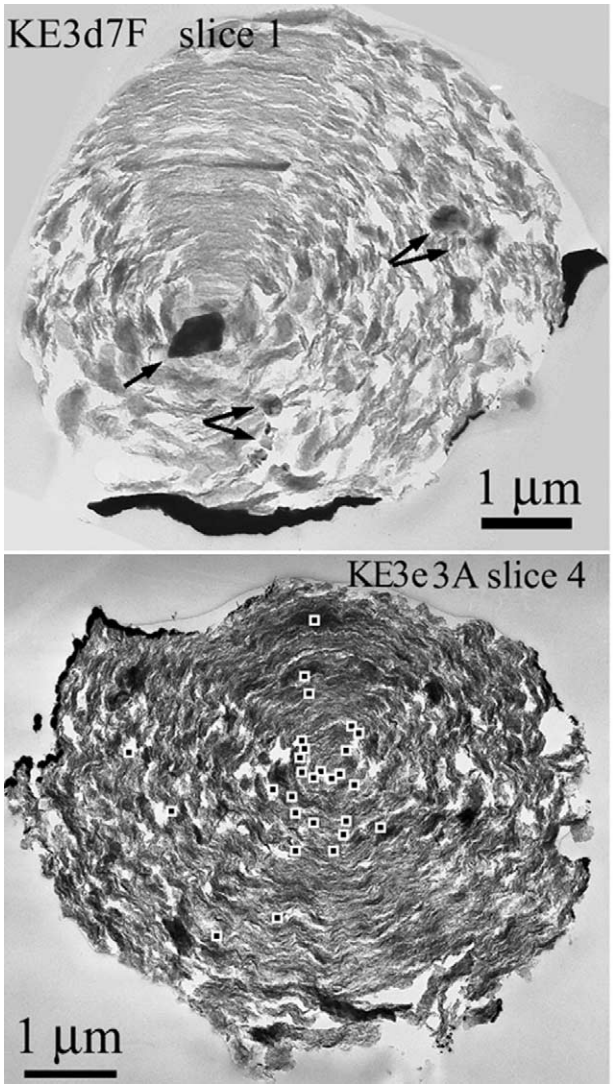

Fig. 2. Bright-field TEM images of 70-nm-thick ultramicrotome slices of SN graphites KE3d7 (top) and KE3e3 (bottom), both showing concentric layers of turbostratic graphite. Microtoming tends to shred layers parallel to the slicing direction, but leaves intact layers perpendicular to it (slicing direction is vertical in these images). Internal grains are present in both slices. The KE3d7 slice contains several large TiC crystals (indicated by arrows), one ~0.5 μm in size, whereas the KE3e3 slice contains 28 TiCs (nanometer-sized and not visible at this scale, but indicated by a black square inside a white symbol). The dark material seen partially bounding the graphites is gold deposited on the graphite during ion microprobe analysis. Slice numbers are for identification purposes and do not indicate slicing sequence.

in some cases these interfered with accurate quantization of these elements within the internal grains. Although all of the KE3 graphites studied were structurally and chemically similar, they differed in the type and abundance of their internal grains, as discussed below.

3.3. Internal Grains Within KE3 Graphites

The types of internal grains found within the low-density graphites are: 1) titanium carbides (TiC, a = 4.39Å fcc), 2) TiC/Fe grains, which are TiC grains with attached iron subgrains (either kamacite or taenite), and 3) kamacite as independent grains not associated with TiC. Table 2 summarizes the properties of these internal grains. The type and number of internal grains are tabulated, along with the abundance (in volume ppm), geometrical mean size, fraction of TiCs with partially amorphous rims, and average major element ratio (V/Ti atomic ratio) of the internal TiCs.

All SN graphites (exclusive of e4 and e8) contained internal TiCs, although the graphites showed great diversity in the TiC abundance and other TiC properties, such as geometrical mean size and chemical composition. The TiC abundance varied by ~2 orders of magnitude among the various SN graphites (25–2400 ppm). As we discuss later, the TiC grains likely formed before the graphite, so these graphites were apparently very efficient at scavenging previously formed dust grains as they grew; for example, as many as several hundred separate TiCs were found within the 6-μm graphite spherule e11. Figure 3 shows that the TiC grain size distributions among graphites are quite variable, with the average geometrical mean TiC size ranging from 30 to 232 nm. This size variation is also evident in the two graphite sections compared in Figure 2. Certain graphites, despite having similar total TiC abundance (Table 2), had quite different grain size distributions (e.g., d7 and e15; e3 and e6). This is also shown in the grain size histograms (Fig. 3), where the abscissa has been scaled in proportion to the diameter of the original graphite to minimize any dependence on the number density of the gas from which a given spherule grew. No obvious scaling relationship is evident between the size of the graphite and the average size and size distribution of its internal grains. The sharp decrease of TiC frequency towards smaller sizes seen in most graphites is a real feature that occurs substantially above the size limit at which grains are no longer detectable by the methods used in this study. No internal TiCs were detected in graphites e4 and e8 (with normal oxygen isotopic ratios but large carbon anomalies); however, only a few sections of these graphites were available for examination.

EDXS measurements of the TiCs showed the presence of Ti, V, and C, often along with other trace elements (O, Mg, Al, Si, P, S, Ca, Cr, Fe, and Ni). TiC and VC are isostructural. Both are NaCl-type structures with C at interstitial sites, allowing V to exist in solid solution within the TiC (up to the solubility limit of 34 at. % V at high temperatures; Upadhyaya, 1996). V was always found in these TiCs, with a volume-weighted mean V/Ti atomic ratio of 0.10 averaged over all TiCs, which is 83% of the solar V/Ti ratio of 0.122 (Anders and Grevesse, 1989). Several graphites had average V/Ti ratios substantially lower than this value (61% and 64% of solar in d7 and e3), whereas others had average V/Ti ratios in excess of the solar value (e7 and f542; Table 2). As shown in Figure 4, there were also significant variations about the mean V/Ti ratios (σ/μ = 7% to 30%, where σ is the standard deviation and μ is the mean) among TiCs found within the same graphite, demonstrating a real variation in the degree to which V was present in solid solution (analytical uncertainty of an individual measurement ≈2%). Si and Fe (5 and 1.5 at. % on average) were the most abundant trace elements, although some signal from the graphite background may have contributed. Other trace elements were not measurable in most TiCs or in the graphite, but were occasionally present in significant amounts in certain TiCs. The

Table 2. Summary of internal crystals within SN graphites.

Graphite #	Internal grains studied	TiC ppm by volume	TiC geometric mean size (nm)[a]	% rimmed TiCs	Average V/Ti atomic ratio in TiC[ac]
d7	21 TiC	2400	232 ± 130	50	0.072 ± 0.006
e7	3 TiC	140	122 ± 8	(66)[b]	0.138 ± 0.01
e10	55 TiC 1 kamacite	1000	187 ± 95	31	0.109 ± 0.02
e15	86 TiC	2300	76 ± 32	51	0.099 ± 0.03
f331	15 TiC	290	126 ± 48	25	0.086 ± 0.01
f542	1 TiC	25	84	(100)[b]	0.200 ± 0.004
e3	149 TiC, 2 TiC/Fe 1 kamacite	950	38 ± 19	6	0.072 ± 0.04
e6	28 TiC, 8 TiC/Fe 1 kamacite	992	136 ± 55	45	0.101 ± 0.02
e11	262 TiC, 70 TiC/Fe	840	30 ± 9	21	0.102 ± 0.03
f131	5 TiC 1 TiC/Fe	110	92 ± 17	20	0.127 ± 0.034
e4	2 kamacite	n/a	n/a	n/a	n/a
e8	None	n/a	n/a	n/a	n/a

[a] The geometrical mean size and V/Ti ratio are reported with the standard deviation of the distribution of measured values.
[b] Lacking in statistical significance due to the small number of grains.
[c] Solar V/Ti = 0.122 (Anders and Grevesse, 1989).

maximum abundances of these elements (in at. %) were: Mg (4.9%), Al (7.5%), P (4.3%), S (1.1%), Ca (1.9%), Cr (1.0%), Fe (12%), and Ni (1.3%). In contrast to the denser KFC1 graphites from Murchison studied by Bernatowicz et al. (1996), no Zr-Ti-Mo carbides were observed in the KE3 SN graphites. As noted in the "Introduction," the presence of such refractory carbides in KFC1 graphites indicated s-process enrichments of Zr and Mo of at least 30 times their solar proportions. Therefore, the absence of these carbides in KE3 SN graphites indicates that significant s-process enrichments above solar proportions were not present in the regions of the SN outflows from which the KE3 graphites formed.

TiC morphologies revealed variable degrees of weathering. Most TiCs (~90%) were euhedral to subhedral, with primary growth faces somewhat corroded but still clearly defined (Fig. 5a,b). There were also a few anhedral grains, some of which showed extensive internal disorder (Fig. 5c). However, the smaller grain size distributions (seen in e3 and e11) cannot simply be due to the breakup of larger grains, because the original grain sizes are still evident from the preserved primary growth faces. Some TiCs were surrounded by an amorphous or nearly amorphous rim layer 3–15 nm thick, partially or completely enveloping the grain. These rimmed grains were present in all of the SN graphites with internal grains, and constituted up to nearly half of the TiC population in several graphites (d7, e6, e7, and e15; Table 2). The rims were clearly evident when the TiC crystal was tilted to a high-symmetry crystallographic zone at intermediate magnifications. Rimmed TiCs were more difficult to quantify by this means in graphites having populations consisting of numerous small TiCs (e3 and e11; Table 2). Figure 5d–f shows several TiCs and a kamacite grain with partially amorphous rims of thickness 3–15 nm. At higher magnifications, the rimmed regions in some grains were found to be at least partially crystalline, as lattice fringes from the crystal were still discernable in the rim (T. Daulton, personal communication, 2002). Rims in other grains were more disordered, showing "nanometer-scale ordered domains within an otherwise amorphous rim" (Bernatowicz et al., 1999). EDXS measurements on some of the rimmed grains showed enrichment of iron (from 2× to 7× higher) in the rimmed region in comparison to the center of the grain. Other trace elements (P and Ca) were also typically higher in rimmed grains than unrimmed TiC grains.

It is important to note that the presence or absence of amorphous rims on TiCs and the degree of TiC corrosion were not correlated with distance of a given crystal from the center of the graphite. Moreover, the rimmed and anhedral TiCs had the same general spatial distribution within a given graphite spherule as the nonrimmed, euhedral and subhedral TiCs. These observations indicate that the surface features (corrosion, rims) of internal TiC crystals are not artifacts of the chemical processing used in making the KE3 graphite separate, nor are they the result of chemical or physical processing of the graphite itself subsequent to its formation. Rather, these features must have developed before the incorporation of TiCs into the graphites (see "Discussion").

3.3.1. Iron phases epitaxially grown onto TiC

In a subset of the SN graphites studied (4 of 10), iron-rich subgrains were found attached to the faces of some internal TiCs (TiC/Fe grains in Table 2). Such grains occurred with variable frequency, with 8 found in e6 (22% of TiCs), 70 in e11 (21% of TiCs), 2 in e3 (1% of TiCs), and 1 in f131 (~1/6 of

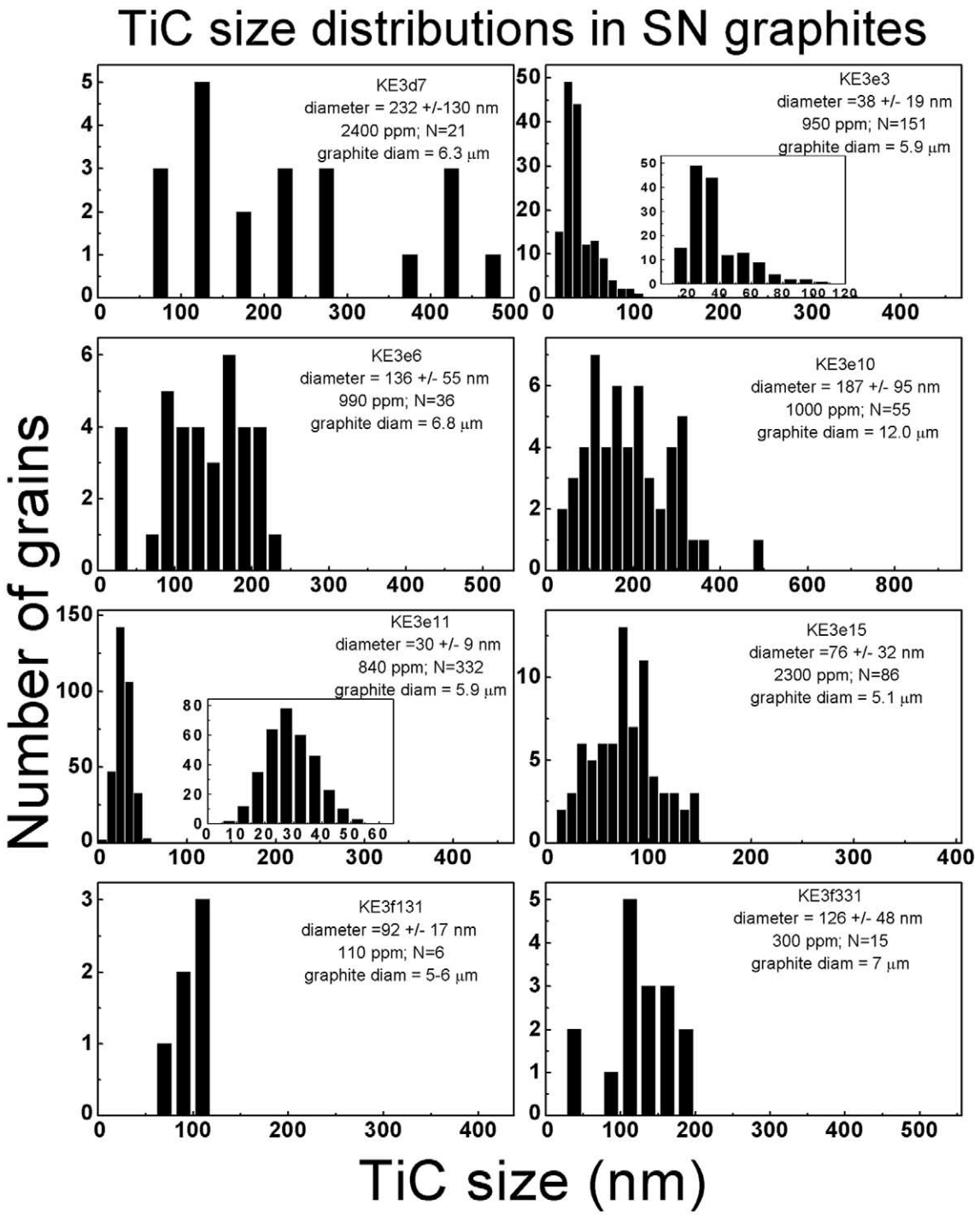

Fig. 3. Internal TiC grain size distributions in various SN graphites (including those TiCs with iron subgrains). The histogram abscissas (size) are scaled in proportion to the diameter of the graphite spherule to eliminate dependence of TiC size on gas density. The TiC mean diameter, abundance, and number of grains studied, as well as graphite spherule diameter, are indicated.

TiCs). In nine cases, multiple iron subgrains were found on the same TiC (see Fig. 5b). The iron subgrains ranged from 8 to 76 nm in diameter, and typically were considerably smaller than the TiCs to which they were attached. The largest iron subgrains (~30 nm mean diameter) were found in e6, whereas in the other three SN graphites the subgrains had a mean diameter of ~15 nm. From electron diffraction data, the iron subgrains were found to be mostly bcc kamacite, along with several fcc taenite grains (2 in graphite e6 and 1 in e3). The composition of the iron subgrains, as determined by EDXS, was only Fe and

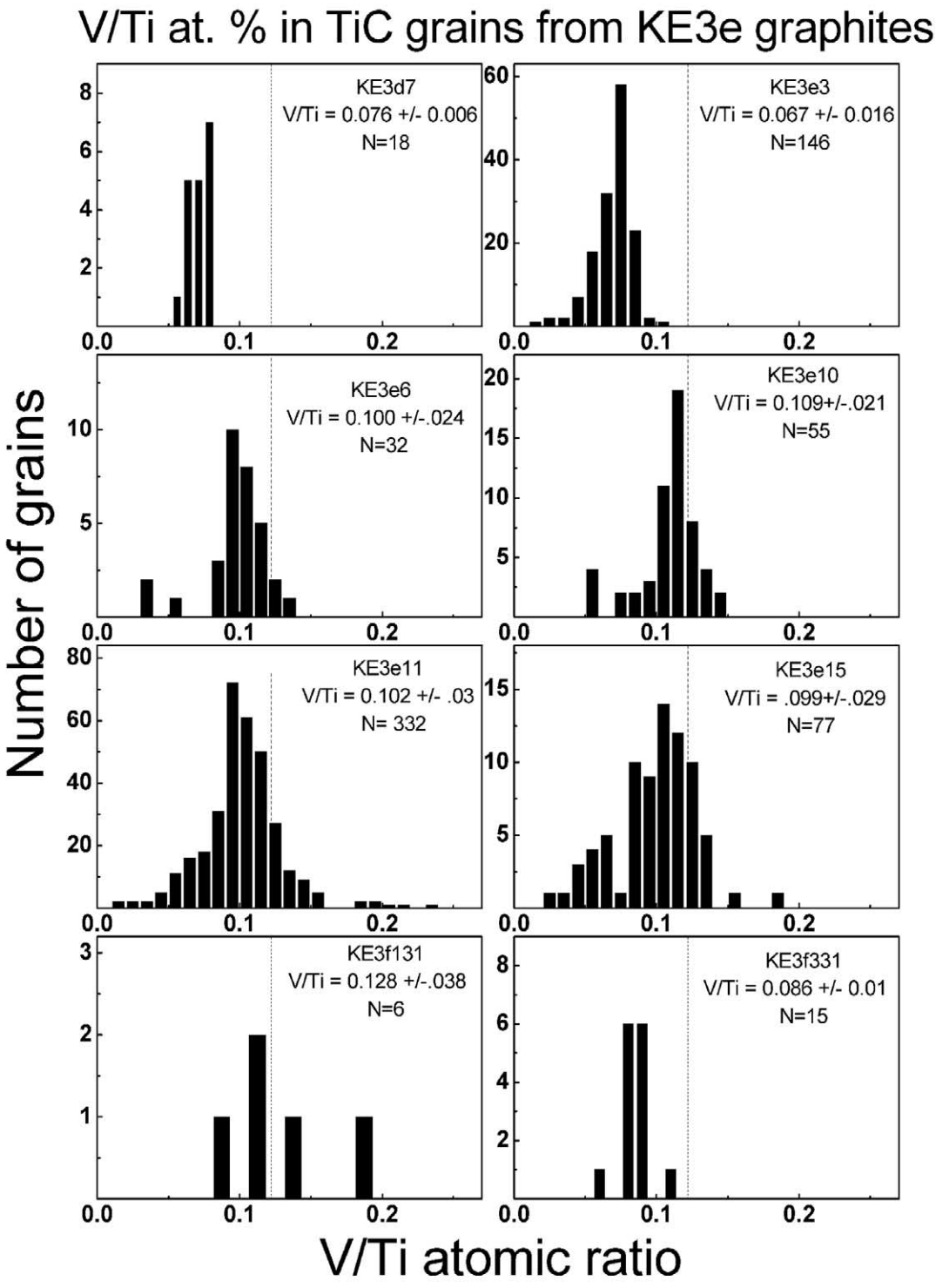

Fig. 4. The distributions of the major element ratio V/Ti (at. %) in TiCs from SN graphites. The average V/Ti ratio (along with the 1σ error) and the number of grains within each graphite are indicated. The solar V/Ti ratio (0.122; Anders and Grevesse, 1989) is indicated by the dashed line in each panel.

sometimes Ni, along with occasional Ti, V, and C signals most likely originating from the nearby TiC. Other siderophile elements (Cr, Mn, Co, etc.) were not detected. Graphite e11 had numerous kamacites on TiCs with an average composition of $Fe_{97}Ni_3$, although some were pure metallic α-iron ($<$0.3 at. % Ni). Higher nickel contents were observed in the kamacite grains from other SN graphites, as much as 28 at. % Ni, considerably in excess of the maximum equilibrium Ni solu-

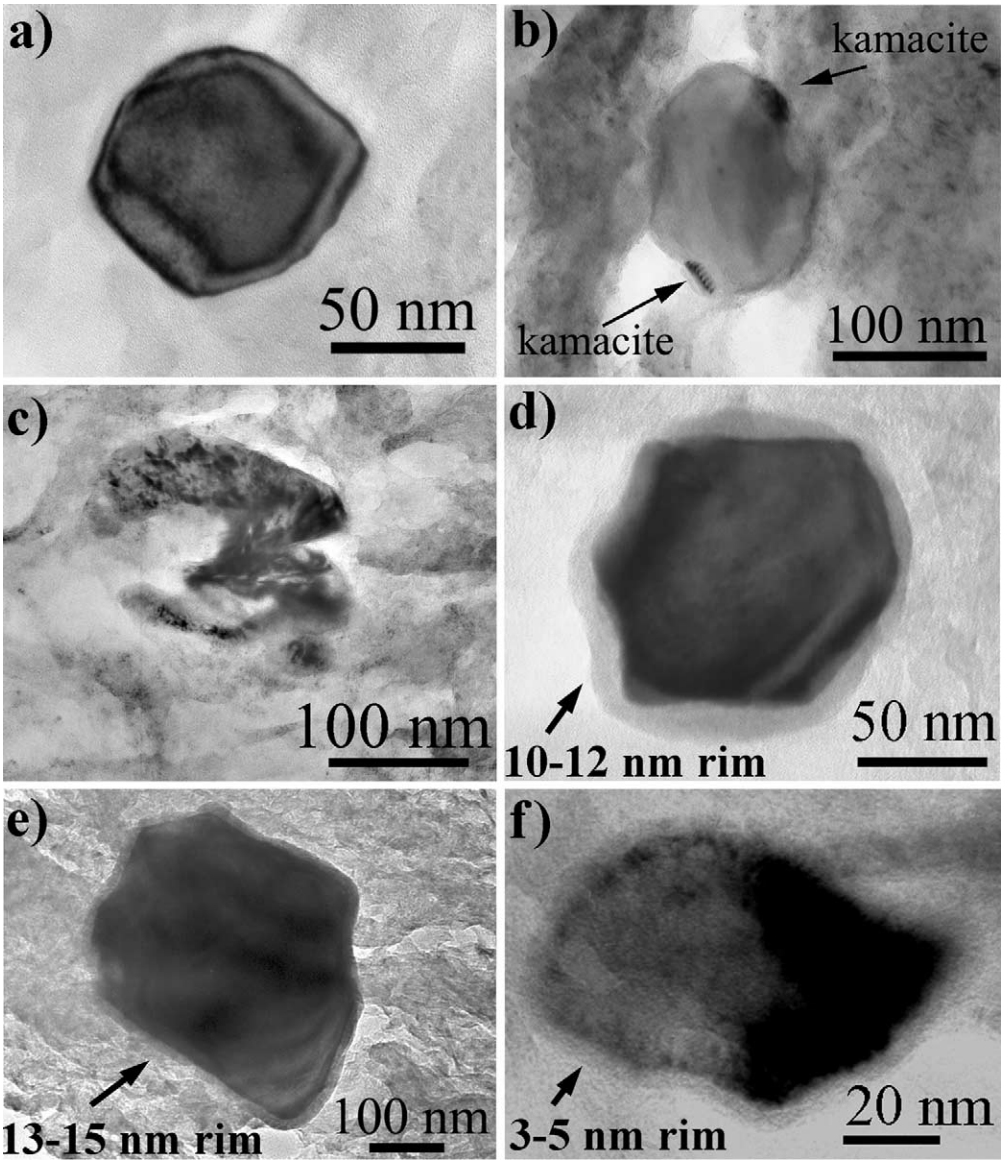

Fig. 5. TEM bright-field images of various internal grains of KE3 graphites: (a) euhedral TiC from KE3e6 (the light and dark bands are fringes due to decreasing thickness of the crystal towards its boundary); (b) subhedral TiC from KE3e6 with two kamacites attached to opposite (111) TiC faces; (c) anhedral grain from KE3e10; (d) rimmed TiC from KE3e7; (e) rimmed TiC from KE3e10; and (f) rimmed kamacite grain from KE3d8 (Bernatowicz et al., 1999). The thickness of the partially amorphous rims on d–f (as indicated on images) ranges from 3 to 15 nm.

bility of ~7% in kamacite (at ≈500°C). The average nickel content of the kamacite grains was 15, 17, and 24 at. % Ni in SN graphites e3, f131, and e6, respectively. We note, however, that such excesses above the equilibrium Ni concentration are not uncommon in synthetic kamacites (Chaudhuri et al., 1972; Ushakov and Litvintsev, 1976). The taenite grains (2 in e6 and 1 in e3) had even higher Ni contents (45, 77, and 60, at. % Ni, respectively).

The orientation relationship between the kamacite subgrains and the TiCs was determined from electron diffraction patterns, and this relationship gives information as to the origin of these composite TiC/Fe grains. If epitaxial growth occurred between TiC (4.39Å fcc) and kamacite (2.87Å bcc), small lattice mismatch and close angular alignment are expected between pairs of low index planes in the two crystals. However, such conditions would likely not be found between two grains that nucleated independently and later became accidentally attached. From the list of atomic plane spacings in these crystals (TiC and kamacite), the smallest possible lattice mismatch is 6–8%, for the (200)fcc//(110)bcc, (220)fcc//(200)bcc, and (222)fcc//(211)bcc planes. The first of these sets of planes, namely (200)fcc//(110)bcc, were found to be parallel (within ≈1.5°) in 11 of the 14 instances where an attempt was made to determine the orientation relationship between the phases. To completely specify the orientation relationship (and eliminate rotational ambiguity), a set of parallel zones (often low index zones) are required along with the set of parallel planes. In the above cases, several different sets of parallel zones were found, in-

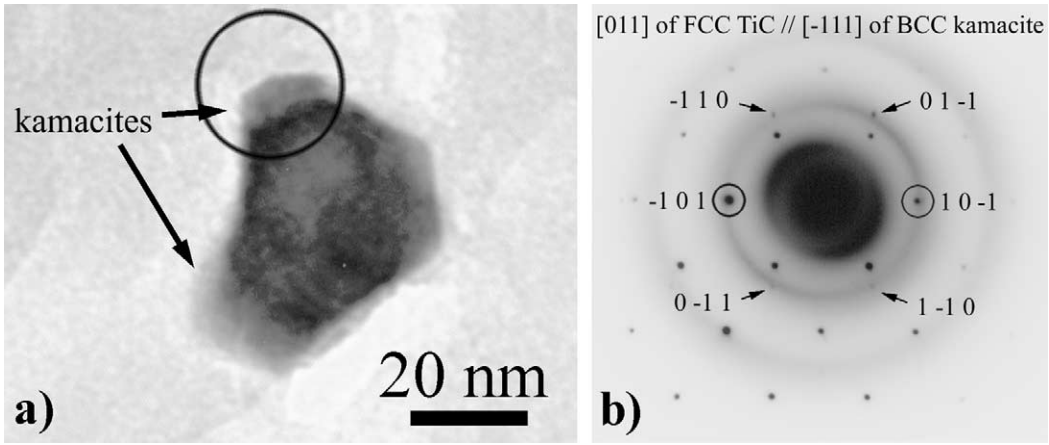

Fig. 6. (a) Bright-field image of a TiC/Fe composite grain from KE3e11 and (b) corresponding SAD pattern showing orientation relationship between TiC and kamacite. The circle on the image in (a) approximately indicates the area selected for the diffraction pattern. In the SAD pattern, the darker array of spots is from the [011] zone of the TiC phase, whereas the faint spots (indicated by the arrows and indices) are from the kamacite subgrain. The circled spots in (b) indicate the position of overlapping diffraction spots from the (200) fcc TiC and the (1 0 −1) bcc kamacite planes. Although not visible in image contrast at this orientation, the two kamacite crystals are present only on the upper and lower (111) TiC faces and do not envelop the grain.

cluding [011]fcc//[111]bcc, [001]fcc//[001]bcc, and [001]fcc//[011]bcc. However, in four of the above cases further alignment of a parallel set of zones was not found, possibly due to the tilt limitations of the TEM stage.

Figure 6 shows a bright-field image and diffraction pattern (of the circled region) from a composite TiC/metal grain found in graphite e11, with two attached kamacites on different {111} faces of the TiC. Indexing of this SAD pattern and separate microdiffraction patterns at this orientation revealed nearly perfect in-plane alignment of the (200)TiC and (1 0 −1)kamacite crystal planes (circled pair of diffraction spots in the figure), and that the [011]fcc zone of the TiC is parallel to the [111]bcc kamacite zone. The diffraction spots from this interface (slightly counterclockwise from vertical in the SAD figure) show that the crystal planes that meet here, namely (111)TiC and (110)kamacite, are slightly misoriented by 4.3°, a condition mandated by the perfect in-plane alignment of the (200)TiC and (1 0 −1) kamacite planes.

Figure 7 shows a larger composite TiC/metal grain from graphite e6, with a kamacite attached to a (200) TiC face. In the SAD pattern, the darker unlabeled spots are from the {200} planes of the TiC, and the faint spots (labeled with indices) are from the {110} kamacite planes. This patterns shows that the (200) TiC plane is parallel to the (110) kamacite plane and that the [001] TiC zone is parallel to the [001] kamacite zone. This particular orientation relationship shows minimum lattice mismatch (≈6%) and good alignment (within 1°) of the crystal planes, both in-plane and at the interface plane. In two other orientation relationships (2 of 14), the (220)fcc plane was found parallel to the (200)bcc plane, another set of planes with the same small lattice mismatch. Here, the [011]fcc and [001]bcc zones were parallel as well. In another of the orientation relationships that was determined, the [011]fcc zone was found parallel to the [001]bcc zone, although no perfect alignment was found between sets of crystal planes. The (111)fcc was 3.6° from the (110)bcc and the (220)fcc 8.8° from the (200)bcc,

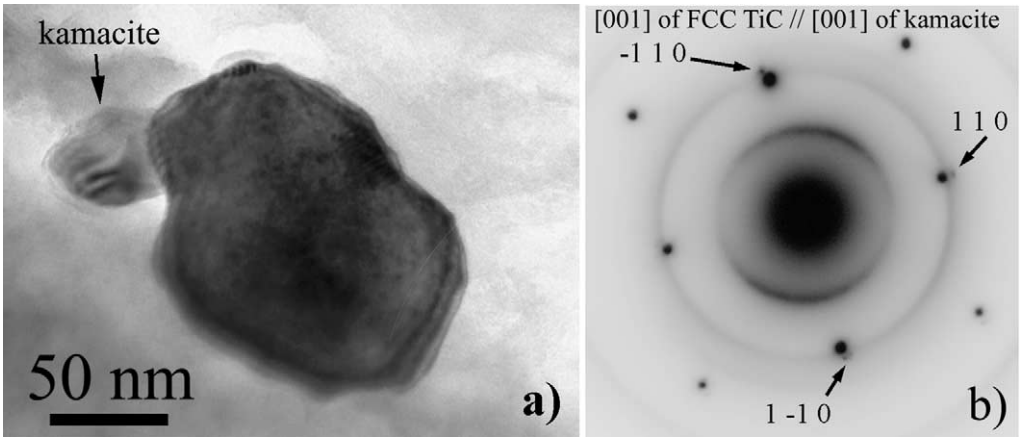

Fig. 7. (a) Bright-field image of a TiC/Fe composite grain from KE3e6 and (b) corresponding SAD pattern of the [001] fcc TiC zone along with extra spots (labeled with arrows) from the [001] bcc zone of kamacite.

so considerable misfit was present within the interface plane itself. Despite this anomalous case, in 13 of 14 cases close angular alignment (within 1.5°) was found between a set of planes that had the minimum amount of lattice mismatch, a clear indication that the relationship between the TiC and kamacite is epitaxial.

As we will argue later (see "Discussion"), the evidence favors the conclusion that the FeNi phases condensed on the faces of preexisting TiCs, creating the epitaxial relationship between the two phases. The kamacite phase mimics the orientation of the substrate (TiC) layer by aligning lattice planes within the interface plane itself, and by aligning the planes at the interface between the two phases. Also, it is not accidental that the most commonly observed set of parallel planes ((110)bcc//(200)fcc) also have the highest lattice point densities of the planes capable of an epitaxial relationship. This is because crystal faces with higher lattice point densities are commonly found to occur more frequently and occupy a larger area relative to other crystal faces (Haüy's Law). Such epitaxial growth is evidently more favorable energetically than independent nucleation of kamacite from the gas, as few kamacites are found independent of TiCs (see next section).

3.3.2. Independently formed kamacite grains

Despite the prevalence of epitaxially grown iron subgrains (88 separate iron subgrains found on 81 different TiCs, see Table 2), iron grains independent of TiC were found only rarely. Two independent iron grains were found in the graphites containing epitaxial subgrains (one in e6 and one in e3). The e6 grain is a 23-nm-diameter kamacite with composition $Fe_{75}Ni_{25}$, near the ≈30% Ni limit seen in synthetic cast FeNi alloys (Chaudhuri et al., 1972). The e3 grain is a 15-nm independent iron grain of composition $Fe_{95}Ni_5$. Although this is likely a kamacite, the grid section containing the slice disintegrated before a conclusive structural identification could be made. Neither grain was near a TiC, so it is unlikely that such iron grains had broken off during slicing. Two more independent kamacites were found in e10 and d8 (Bernatowicz et al., 1999), which did not contain any TiC/Fe composite grains. These grains were slightly larger (73 nm and 87 nm geometrical mean diameter) than the typical kamacite subgrains, with compositions of $Fe_{85}Ni_{14}Cr_1$ and $Fe_{80}Ni_{17}Cr_3$. Although Cr was not detected in any iron subgrains, it could have been present in very small concentrations (≈1 at. % or less). Such small Cr concentrations would be difficult to detect in TiC/Fe composite grains, as a small Cr-$K_\alpha$peak in the iron subgrains would be masked by the V-K_β peak signal coming from the nearby TiC grain. Some weaker reflections seen in the partially amorphous rim of a kamacite from d8 were indexed as nanocrystalline cohenite (orthorhombic, $(FeNi)_3C$; Bernatowicz et al., 1999). Three of the four independent kamacites showed evidence for 5–10 nm partially amorphous rims surrounding the grains, similar to those seen around the TiCs. These rims are of comparable thickness on both phases, and are also compositionally similar to their host grains, suggesting a physical damage mechanism as the cause for the amorphous rims (see "Discussion").

3.4. NanoSIMS Analyses

The individual internal TiCs in KE3e10 were analyzed in the NanoSIMS to verify that they, like the SN graphites themselves, had anomalous isotopic compositions. With its typical spatial resolution of 100 nm, the NanoSIMS was capable of measuring the C and O isotopic ratios in many of the TiCs (which had ≈200 nm average diameter in KE3e10). The $^{12}C/^{13}C$ isotopic ratios in the TiCs were indistinguishable from that in the surrounding graphite (see Table 1). However, the $^{16}O/^{18}O$ isotopic ratios in the TiCs were more anomalous than in the graphite, showing greater relative excesses of ^{18}O. $^{16}O/^{18}O$ ratios from 14 to 250 were measured in TiCs, whereas the bulk graphite has a ratio of 174 (Stadermann et al., 2003). The large range of measured ratios again suggests that TiCs formed before the graphite and then were incorporated during its growth (as discussed later). Anomalous titanium isotopic ratios were also found in the TiCs from KE3e10 (Stadermann et al., 2003). These results conclusively prove that TiC is a presolar phase that forms in the circumstellar environments of SN.

The NanoSIMS was also useful in identifying nonpresolar phases within KE3e10. Two internal grains have the crystal structure of chromite as determined from electron diffraction in the TEM, with diameters of 71 nm and 222 nm, and both have an approximate composition of Cr_3FeO_4. Here the metal ratio was precisely measured, whereas the oxygen amount is inferred from the crystal structure. The larger chromite was examined in the NanoSIMS, and found to have terrestrial oxygen isotopic ratios, although the surrounding graphite was clearly anomalous in oxygen. This suggests that this grain formed either in the solar system or during laboratory processing. Both of the chromites were found towards the exterior of this graphite (outer 20% of the graphite radius), suggesting that they may have formed from oxidation of iron-rich grains, which could have occurred while the graphites were being isolated from the Murchison carbonaceous chondrite. During the separation procedure, a dichromate solution ($Na_2Cr_2O_7$) was used to remove organic and amorphous carbon. If this solution were to come into contact with a preexisting iron-rich grain, it could oxidize the grain and form chromite. Chromites were also found in the outer regions of other graphites (always in the outer 20% of the graphite radius; a total of 11 chromites in 6 different graphites). The chemical composition of the chromites was predominantly Cr, along with variable concentrations of Fe (3–26 at. %), Al (0–40 at. %), and Mg (0–34 at. %). Some are actually magnesiochromites, isostructural with chromite (8.39Å fcc) but with larger Mg and Al concentrations, maintaining an approximate stoichiometry of $(Cr,Al)_2(Fe,Mg)O_4$ (again only the metal ratios were precisely measured). Although not yet measured with the NanoSIMS, these other chromites (and magnesiochromites) are also likely not presolar grains.

3.5. Correlations Among Properties of TiCs

The large number of internal TiCs in the SN graphites permitted a search for possible correlations among their chemical, morphologic, and other properties. Several trends were observed in some graphites as a function of the distance of the TiC from the graphite center, a rough measure of the time at which the internal grain was incorporated into the graphite.

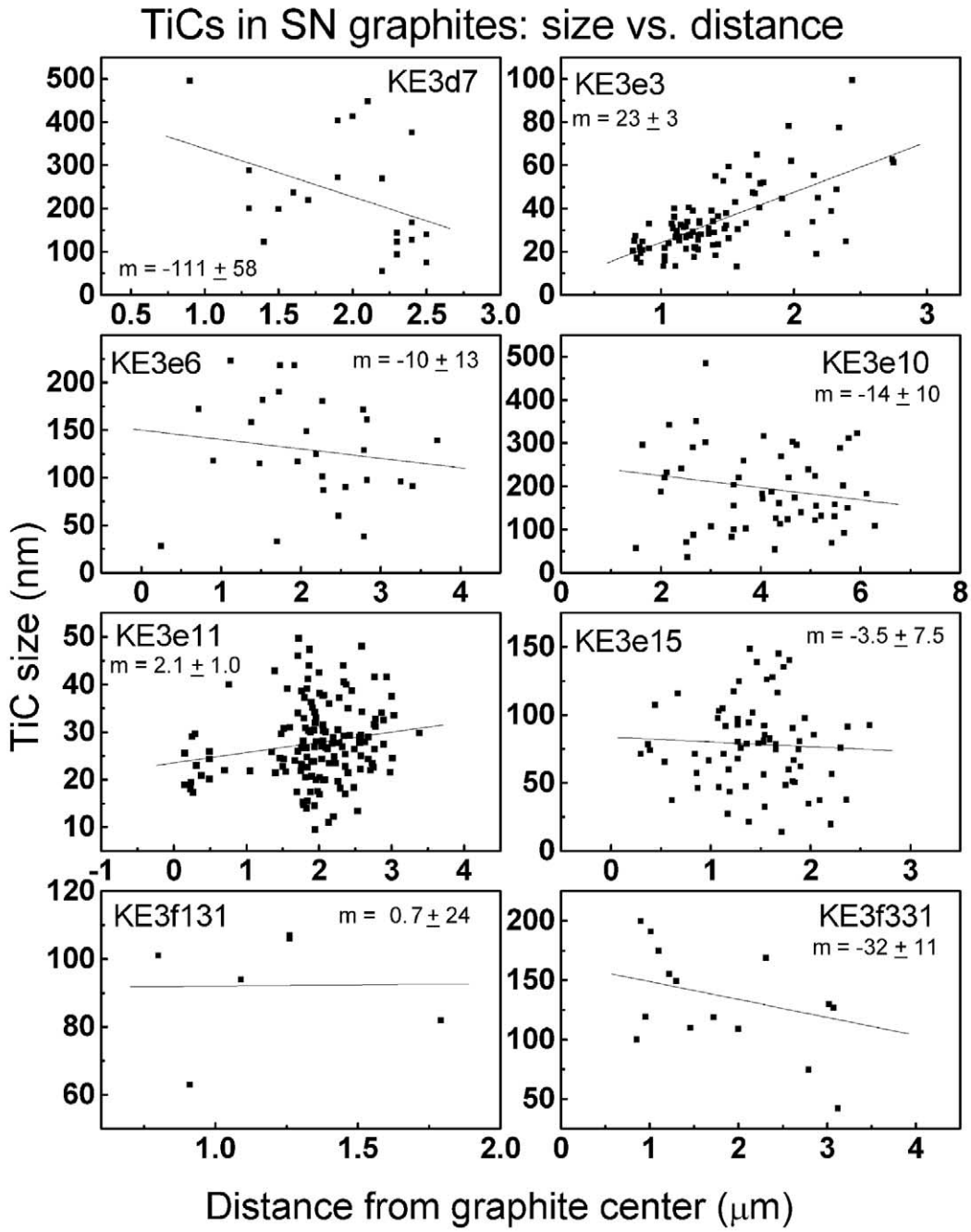

Fig. 8. Size vs. radial distance trends of TiCs within SN graphites. Least squares linear fits are also plotted and the slope (m) and 1σ standard error are indicated in each panel.

Figure 8 displays the size of the internal TiCs vs. their distance from the graphite center in different SN graphites. Most graphites do not show strong correlations between size and distance, suggesting that TiC growth was more or less completed when the graphites began to form, or else that graphite growth was far more rapid than TiC growth. However, one graphite (KE3e3) does show a strong positive correlation between the TiC size and distance from the graphite center, an indication that in this case TiC growth was likely not complete when graphites began to form. Several graphites show weakly negative trends in TiC size vs. distance (d7 and f331), perhaps indicating that TiCs that remained in the gas for longer times were more corroded. As mentioned earlier, the grain morphologies support the idea that TiC corrosion has occurred.

Within many individual graphites, trends are also apparent in the major element ratios (V/Ti at. %) in TiC with distance from the graphite center, and with TiC grain size. Figure 9 shows the V/Ti atomic ratio vs. the radial distance from the graphite center for all graphites containing a sufficient number of TiCs. Clear increases in the relative amount of V vs. radial distance

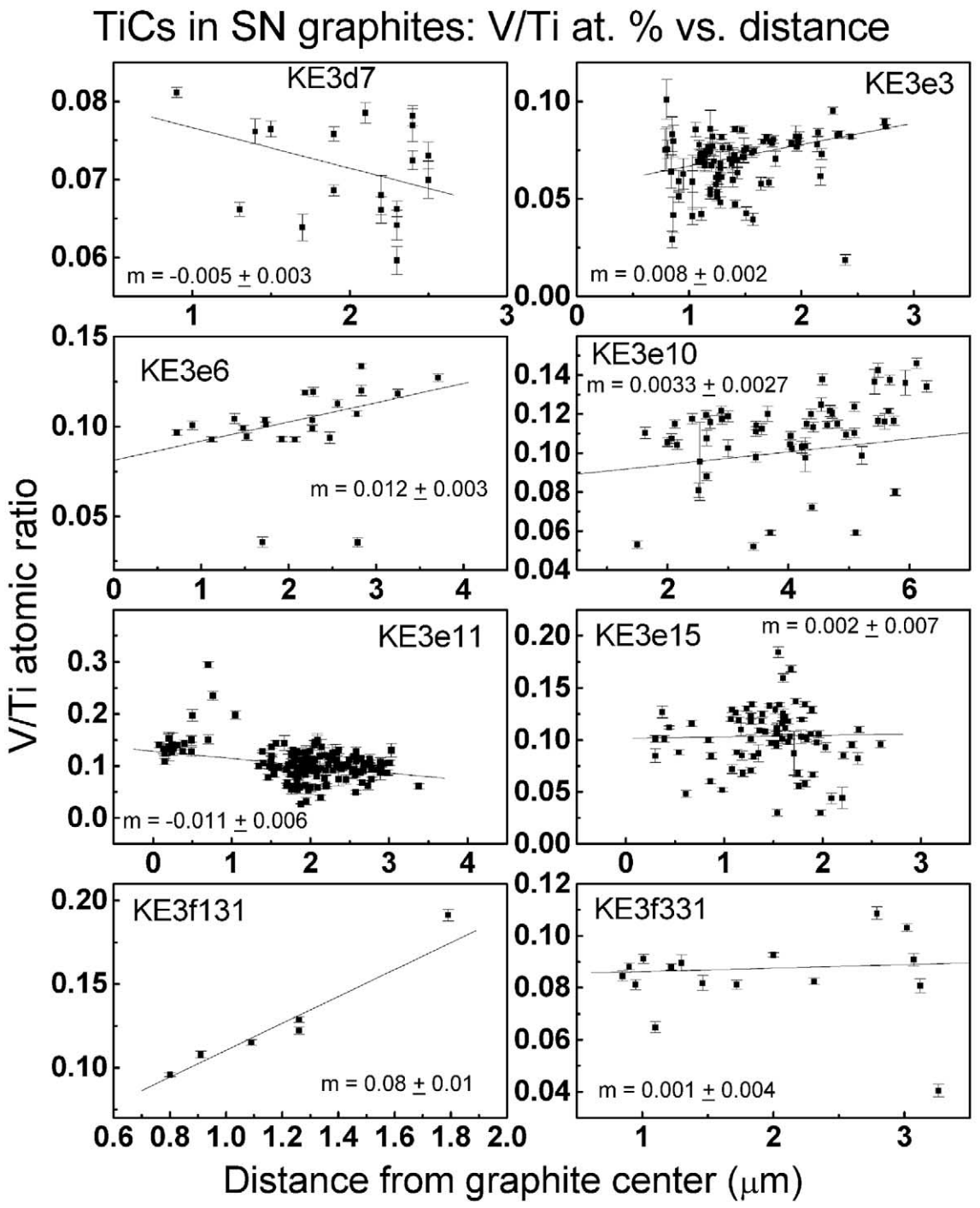

Fig. 9. The V/Ti atomic ratio in TiCs is plotted vs. the radial distance from the graphite center for SN graphites. TiCs containing iron subgrains (in e3, e6, e11, and f131) are plotted along with the other TiCs, and participate in the overall chemical trends. Error-weighted least squares linear fits are also plotted and the slope (m) and 1σ standard error are indicated in each panel.

are seen in several SN graphites (e3 and f131), as well as slight increases in e6 and e10. These positive trends are likely due to chemical evolution of the TiCs in the ambient gas with time. Vanadium carbide, although soluble in TiC, is less refractory and condenses at a substantially lower temperature (cf. Lodders and Fegley, 1995). Thus, TiCs found towards the graphite exterior, which were probably exposed to the gas for longer times and at lower temperatures before capture by the graphite, incorporated more V. The observed trend in V/Ti suggests that this ratio was continually evolving in the TiCs as they were

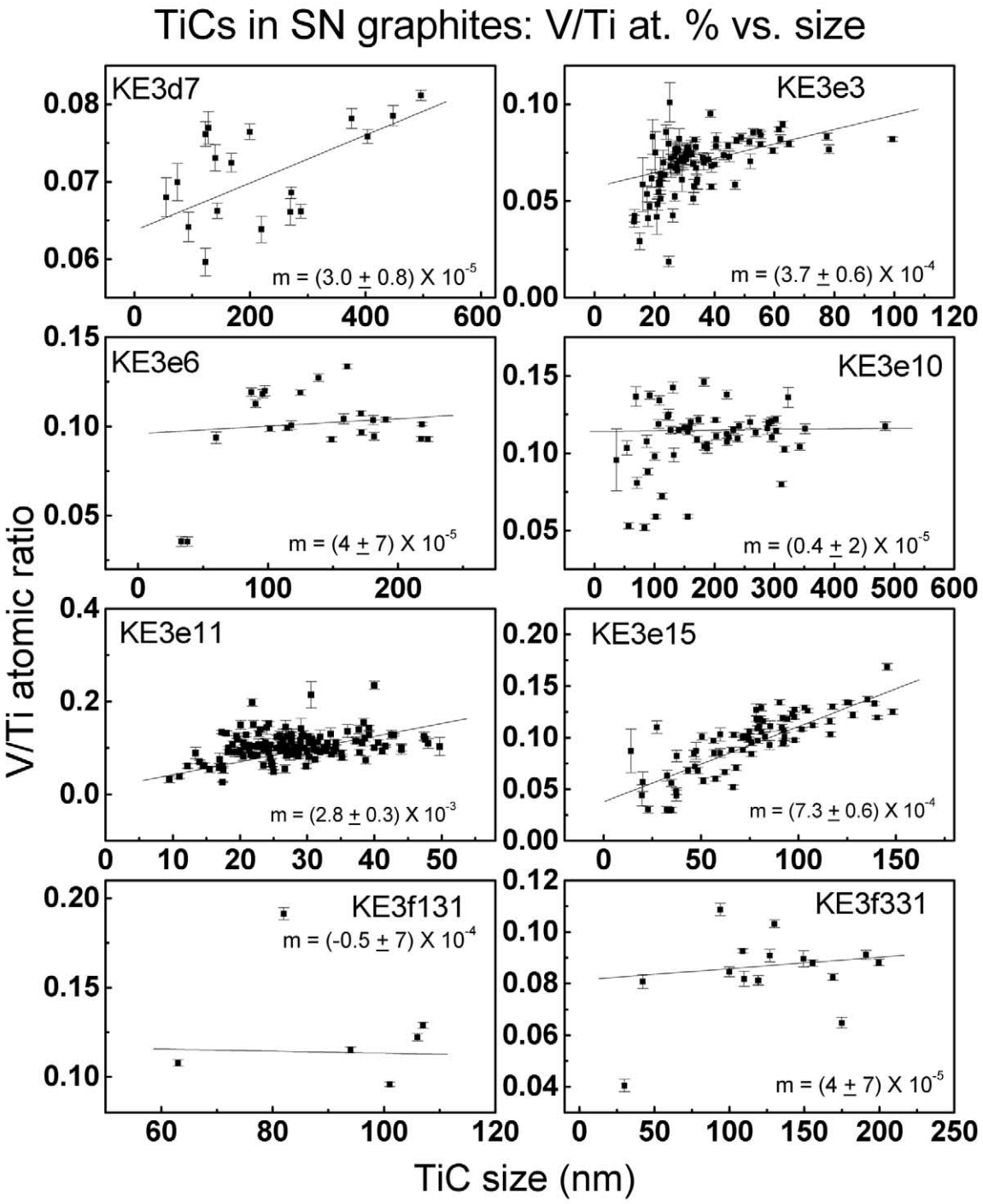

Fig. 10. The V/Ti atomic ratio of the TiCs vs. TiC grain size for SN graphites. Error-weighted least squares linear fits are also plotted and the slope (m) and 1σ standard error are indicated in each panel.

being incorporated into the graphite, but ceased evolving once the TiC was trapped by the graphite.

The V/Ti ratio of internal TiCs typically increases as a function of TiC size in a given graphite, with smaller grains ($<$150 nm) having lower V/Ti ratios than larger ones (Fig. 10). This increase is most pronounced in graphites with smaller TiCs (such as e3 and e15; Fig. 10 and Fig. 3), where the V/Ti ratio rapidly increases with size, appearing to asymptotically approach a limiting value towards larger sizes. SN graphites with predominantly larger TiCs either showed a weak increase with size or no trend. The lower V/Ti ratios measured in small grains were not likely due to EDXS quantization errors, as some small grains with high V/Ti ratios were also found. Unlike the V/Ti vs. radial distance trend, this correlation cannot

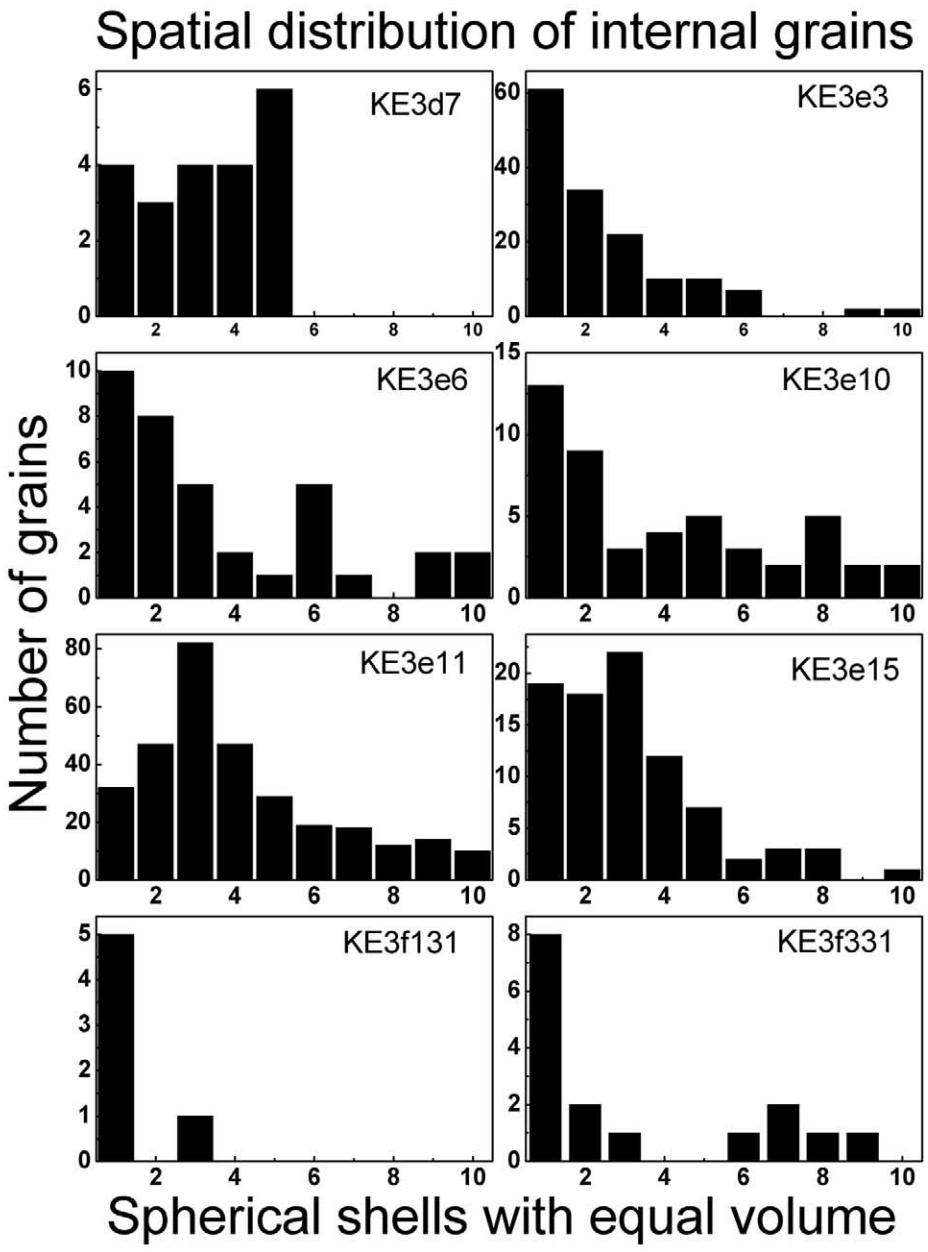

Fig. 11. Histograms showing the number of internal TiCs as a function of distance from the center of various SN graphites, with internal TiCs binned into 10 spherical elements of equal volume. The TiC number density is typically higher towards the interior. For example, the innermost two shells in e10 (20% of the graphite volume) contain 22 TiCs, whereas the outer two shells contain only four TiCs.

be explained simply by the temperature or time dependence of V incorporation, and possible causes for this trend are considered in the "Discussion" section.

In the SN graphites there is typically a decrease in the number density of internal grains as a function of increasing radial distance (therefore at later graphite condensation times) from the graphite center. This phenomenon is shown in Figure 11, where we have analytically divided each graphite spherule into 10 spherical shells of equal volume and counted the number of TiCs found in each shell. The number of internal TiCs is clearly higher in the inner shells towards the graphite center. This trend is also obvious in the slice of KE3e3 shown in Figure 2. If, as we have argued above, the TiCs were already present in the gas and were accreted onto growing graphite spherules, the mechanism of their capture is essentially the same as that of the carbon molecules contributing to graphite growth. That the relative numbers of molecules and TiCs captured in a given time interval is not constant requires a change in either their relative abundance or their relative sticking probabilities. One possibility is a progressive change (particularly an increase) in the effective sticking probability of carbon molecules onto graphite, relative to TiC, over the time

of graphite growth. This is most simply explained if we assume that the sticking probability of the carbon molecules contributing to graphite growth increases with decreasing ambient temperature, resulting in a smaller number density of TiCs in graphite at greater spherule radii. Alternatively, the relative abundance of TiCs in the gas could become smaller over time. If the TiCs had a substantially higher sticking probability than carbon when incident on a growing graphite, then the relative TiC concentration in graphite would be substantially higher than the initial concentration in the gas. After a significant number of graphites had condensed, the gas in a closed system would become depleted in TiCs and could cause the observed trend in TiC density vs. radial distance.

Despite the higher number density of TiCs toward the interior of the SN graphites, there was usually no evidence of TiCs acting as heterogeneous nucleation sites for the graphites. In a number of instances (e.g., e10, e6, f131, and f542), there were clearly no TiCs near the graphite center, precluding the possibility of heterogeneous nucleation of graphite on TiC. However, since only $\approx$ 1/3 of the graphite volume could be observed after slicing, evidence of heterogeneous nucleation may have been originally present but not observable in the slices available for study. Only graphite d7 clearly contained a large central TiC which may have served as a heterogeneous nucleation site for the graphite. In other graphites with numerous small grains (e3 and e11), the grain number density is so high that the determination cannot be made. TiCs were observed in various slices near the centers of these graphites, but given the large overall TiC number density, the position of the TiCs may be coincidental and not necessarily indicative of heterogeneous nucleation.

4. DISCUSSION

The morphology of some TiCs suggests that they formed before the graphite containing them. Although most grains were euhedral, the TiCs often showed extensive corrosion, in extreme cases leaving anhedral grains with no primary growth faces. Partially amorphous rims (Fig. 5d–f; Table 2) were also found surrounding some internal grains (both TiC and kamacite). The most plausible explanation for the corrosion and the rims is that these grains were exposed to external physical or chemical processing, or to both, before they were encapsulated in and protected by the graphite. The more pristine grains present also likely formed before the graphite, but experienced less weathering before incorporation. Along with morphologic differences, substantial variations are seen in the major element ratios (V/Ti) and in trace element concentrations among TiCs from the same SN graphite. These observations give further evidence that the TiCs formed before the graphite. If this were not the case (e.g., TiC formation via exsolution from the graphite), the considerable chemical variations (often seen in TiCs within 1 μm of each other in the same graphite slice) would likely not occur. Overall, the variations in both internal grain composition and morphology together show that the internal grains formed first and had different histories before incorporation, suggesting that some degree of mixing in the SN ejecta occurred. The graphite acts as a "time capsule," capturing and preserving a sample of the grains present from the early stages of condensation in the expanding SN ejecta. The observed morphology and the chemical and isotopic compositions of these internal grains are primary features of these higher temperature condensates. Analysis of these internal grains thus gives information about the history of condensation in the SN ejecta.

The existence of iron–metal subgrains on internal TiCs adds further detail to the phase condensation sequence, providing another constraint on condensation in SN ejecta. It follows from the arguments presented above that the TiC/Fe composite grains also condensed before graphite. However, the epitaxial relationship between the TiC and Fe-rich phase alone does not conclusively show which phase condensed first. That TiC formed before the iron–metal phases is clear, however, given several facts: 1) multiple iron subgrains have been found epitaxially grown on the same TiC (see Fig. 5b), which logically can only occur if the TiC formed first; and 2) TiC was often found independent of iron–metal, whereas iron–metal was found almost exclusively on TiC. The latter point suggests that heterogeneous nucleation of iron–metal on refractory grains was generally necessary for it to form before graphite. The condensation of iron subgrains on TiCs may have been more or less complete before the graphite formation began in e6 and e11, as no trends are seen in their frequency as a function of distance from the graphite center. Alternatively, the growth of graphite may have been far more rapid than the continued growth of iron, effectively quenching the growth of iron subgrains.

The inferred phase condensation sequence acts as an important constraint on any thermochemical modeling of condensation in circumstellar environments. Formation of refractory TiCs before graphite or iron–metal phases is not surprising, as the equilibrium condensation temperature of TiC is predicted to be higher than graphite or the iron–metal phases over a relatively wide range of pressures and C/O ratios in a gas of otherwise solar composition (Lodders and Fegley, 1995). However, condensation of iron–metal phases before graphite (only seen in a subset of SN graphites) is not universally expected, and places a more rigid constraint on the conditions in which the TiC/Fe composite grains and the graphites condensed. It must be noted that accurate predictions of the condensation sequence are not trivial, given the complex interplay between various possible chemical reactions, and especially because the gas composition is not well known. Previous thermodynamic modeling of a gas with otherwise solar composition only predicts metallic iron condensation before graphite at low C/O ratios (e.g., $1 < \mathrm{C/O} < 1.05$) accompanied by high gas pressures ($>10^{-3}$ bars; Lodders and Fegley, 1995). However, under such conditions, SiC would also condense before graphite and likely would be seen as internal grains. Therefore, the condensation of iron–metal phases before graphite (in a subset of the SN graphites) suggests that, in this case, the gas composition is not solar, but relatively enriched in iron. Current SN models do predict a slight overproduction of iron relative to the amount expected in a gas of solar composition (Meyer et al., 1995). However, the overproduction is due to the synthesis of new iron in the interior (Ni shell), and the outer carbon-rich shells (He/C and He/N), where graphite formation likely occurs, are depleted of iron by s-processing during presupernova evolution. This may be a further indication that some mixing of supernova ejecta has occurred, bringing some of the excess iron into the graphite-forming region. It is also possible that iron forms before graphite because graphite requires a greater supersaturation before condensing.

Large variations were found in the overall TiC abundance among the SN graphites. The range in TiC abundance (relative to graphite) likely reflects variations in the C/O ratio of the gas from which the individual SN graphites condensed. Although graphite formation in an oxygen-rich environment has been proposed (Clayton et al., 1999), the graphites studied here most likely formed in environments with C/O $>$ 1, because a plausible case cannot be made for the formation of their internal TiCs in an O-rich gas. In particular, thermochemical equilibrium calculations indicate that for TiC to form in a gas of otherwise solar composition, the C/O ratio must exceed 0.98 (Lodders and Fegley, 1995). In C-rich gases, much of the carbon is likely bound to oxygen in CO, leaving only the excess carbon available to form TiC and graphite. The range of TiC relative abundances measured in these graphites is consistent with such a scenario, and yields reasonable values for the C/O ratio in the gas. Assuming a solar Ti/O ratio, and that all Ti forms TiC and excess C (above that forming CO) forms graphite, C/O ratios from ~1.1 to ~3.0 yield TiC relative abundances relative to graphite that match most of the measured values (110–2400 ppm). Only the lowest measured value (25 ppm in SN graphite f542) would require a substantially larger C/O ratio (near 10). Other factors can also reduce the relative TiC abundance and thus explain lower measured values, namely the Ti abundance in the gas may be lower than the solar ratio or the TiC abundance in graphite may not match its abundance in the gas from which it condensed. The latter case is clearly true for iron, which has a typical measured abundance of ~1000 ppm in graphite, rather low given that Fe is undoubtedly much more abundant than Ti in the gas. The elemental abundance in graphite can be decreased from that in the gas if condensation of a given phase containing the element had not yet gone to completion when graphite formed (likely true for Fe but less so for the more refractory TiC). Also if the gas is being preferentially depleted of TiCs over time, graphites that form later would have a lower TiC abundance. Despite these other factors, the reasonable match between most of the measured TiC abundances in graphite and the values expected from C-rich gases suggests that 1) most Ti had already condensed from the gas as TiC when graphite formed and 2) the TiC grains were efficiently incorporated into the growing graphites.

The sizes of the TiCs (from ~15 nm to ~500 nm) can be used to place a lower limit on the Ti number density in the gas before condensation. We use a growth model wherein the growth rate is proportional to the number density of gas species contributing to grain growth and to the thermal velocity of the condensing species (Bernatowicz et al., 1996; Bernatowicz and Cowsik, 1997; Sharp and Wasserburg, 1995). For unit sticking efficiency, the grain growth rate is:

$$\frac{dr}{dt} = \frac{\mu}{4\rho N_A} n \bar{\nu}$$

with the mean speed $\bar{\nu}$ given by

$$\bar{\nu} = \left(\frac{8kT}{\pi m} \right)^{1/2}$$

Here r is the grain radius, μ and ρ are the molecular weight and density of the solid, T is the absolute temperature, N_A is Avogadro's number, k is Boltzmann's constant, and m and n are the molecular mass and number density of the gas phase species being deposited. Because Ti is far less abundant than C, the Ti number density and thermal velocity will dominate the growth behavior. Assuming a growth time of 1 yr and a condensation temperature T ~ 1800°K, minimum Ti number densities in the gas of $\nu_{Ti} \sim 7 \times 10^4$ to $\sim 2 \times 10^6$ atoms/cc are required to form grains in the size range observed. These number density estimates are not extremely sensitive to either the assumed growth time or sticking coefficient, with a linear dependence on each. The growth time estimate is reasonable, given that dust formation in SN ejecta was observed on this time scale in SN 1987A (Wooden, 1997). In any event, longer condensation times would reduce the required number densities proportionally. The sticking coefficient is likely lower than unity, which would require even greater Ti number densities to form grains of the observed size range. Although the gas composition is not solar, for scale, the pressure range corresponding to the above range of Ti number densities would be ~0.2 μbar to ~5.0 μbar in a gas of solar composition. The inferred minimum Ti gas number densities correspond to minimum TiC grain number densities of $\sim 3 \times 10^{-4}$ to ~0.2 grains/cc, assuming complete condensation of Ti in TiC. From the Ti number densities, we estimate the maximum ratio of mean TiC grain separation distance D in the gas to grain diameter d as $D/d \sim 3 \times 10^5$ to $\sim 1 \times 10^6$. The ratio D/d is relatively insensitive to the Ti number density (ν_{Ti}) in the gas, varying as $\nu_{Ti}^{-1/3}$. This large grain separation means that collisions between same-size TiC grains will be infrequent, with a velocity-independent mean free path of ~0.1 astronomical units (A.U.) between collisions.

There is no simple scaling between the size of internal TiCs and the size of their host graphite, as might naively be predicted if the sizes of both TiCs and graphites depended only on the overall pressure. The absence of a simple scaling relationship indicates that other variables affect grain size, and that the values of these variables differ among the observed SN graphites. First, the number density of TiC nuclei will affect the grain size distribution and the ultimate size to which TiCs can grow. Given the same overall Ti number density, a higher initial nuclei number density will result in a smaller grain size distribution. The sizes of the host graphites will similarly be affected by the initial density of graphite nuclei. Along with the nucleation behavior, the grain sizes of each phase are independently affected by the overall abundance of the condensing atomic species in the gas. It is likely that $\nu_{Ti} << \nu_C$ (where ν_C is the number density of carbon species contributing to graphite growth) for any gas from which both graphite and TiC can condense, so any increase in the Ti abundance in the gas would likely increase the TiC grain sizes without having an appreciable effect on the graphite size. Similarly, an increase in the abundance of excess carbon (higher C/O ratio) would increase graphite grain sizes without changing the TiC size distribution.

The partially amorphous rims (3–15 nm) seen on both TiC and kamacite grains are comparably thick and related in composition to their host grains (Bernatowicz et al., 1999). Given these observations, at least two formation mechanisms may be conceived. The first is physical, suggested by the fact that these rims resemble the solar-wind damage features seen on lunar soil grains, which have ~50 nm thick amorphous rims caused by irradiation with ~1 keV/nucleon (~400 km/s) H and He

ions (Keller and McKay, 1997). TiCs and kamacite grains forming in SN ejecta may also have been exposed to particle irradiation, a kind of "reverse solar wind," due to collisions between the grains and slower-moving parcels of gas. Fingers of gas are ejected at high velocities ($\sim 10^4$ km/s) in SN due to Rayleigh-Taylor instabilities (Wooden, 1997). In such an environment, a drift velocity $\Delta v \sim 100$ km/s between the grains and slower-moving parcels of gas is plausible, being at most only a few percent of the mass outflow speed. A drift velocity of this magnitude is a factor of several less than the solar wind speed, and so less thick damaged regions ($\sim$10 nm) are reasonable. The other possible formation mechanism is chemical, in which these rims are caused by chemical corrosion, if the gas conditions were to change with time to a state in which the TiCs and kamacites were no longer stable. However, this seems less likely given that comparably thick rims are found on compositionally dissimilar phases. Moreover, in the case of KE3e3, where $\sim$6% of the TiCs have rims, the TiC size vs. radial distance trends indicate that most of the TiCs were still growing at the time they were incorporated into their host graphite, so the gas environment could not be simultaneously corroding and growing TiCs.

The significant variations in the V/Ti ratios among TiCs in a given graphite likely reflect the temperature at which each grain condensed, rather than indicating a variation in the chemical abundances in the gas. Vanadium carbide is less refractory than TiC, with a 150°C to 200°C lower condensation temperature over a wide range of pressures (10^{-2} to 10^{-14} bars) and C/O ratios (1.05–4), assuming solar relative abundances (Lodders and Fegley, 1995). The amount of V in solid solution in TiCs will also reflect this temperature dependence. Therefore, TiCs condensing at higher temperatures (above the VC condensation temperature) will likely have lower V/Ti ratios than those condensing later at lower temperatures. The wide V/Ti distributions in TiCs preserved within the SN graphites demonstrate that TiCs do not fully equilibrate with the surrounding gas at lower temperatures. This is physically reasonable, assuming that encapsulation within the graphite prevents further chemical equilibration. However, there is evidence of progressive equilibration of the amount of V in solid solution in TiC before encapsulation in several graphites, as seen in the increasing trend of V/Ti vs. distance from the graphite center. As shown in Figure 9, four graphites (e3, e6, e10, and f131) showed clear increases in the V/Ti ratio of TiCs towards the exterior of the graphite. This implies that as growing TiCs were exposed to the cooling gas they progressively evolved towards higher V/Ti ratios, with TiCs accreted near the end of graphite growth having time to acquire the most V. Thus, the temperature history of the TiCs is to some degree preserved in the V/Ti ratios, yielding further information about the refractory grain condensation process.

Only one SN graphite (e11) showed the opposite trend, a negative correlation between the V/Ti ratio and radial distance (Fig. 9). However, in this case, there were clearly two different grain populations, with higher V/Ti grains grouped near the graphite center (radial distance < 0.8 μm) and lower V/Ti grains towards the exterior (radial distance > 1.35 μm), as well as a pronounced deficit of TiC crystals between the two regions. This gap plausibly represents a temporal cessation of TiC accretion by the growing graphite spherule as it traversed pockets of ambient gas with variable number densities of previously formed TiCs. Thus, the negative trend in e11 may simply be the result of the sampling of two distinct TiC populations with different V/Ti. NanoSIMS isotopic analysis of TiCs within e11 graphite slices are planned to search for any isotopic differences between the two populations. Graphite d7 also showed a weak negative trend, but here the range of measured V/Ti ratios was quite small (0.06 to 0.08) and thus less significant.

Several of the SN graphites (e3, e11, and e15) showed considerably higher V/Ti ratios in larger TiCs (Fig. 10). As the grain size increases, the V/Ti ratio often appears to asymptotically approach a limiting value, possibly the V/Ti ratio of the gas. Since the TiCs in e11 appear to be from two different grain populations, the V/Ti vs. size trend (not to be confused with the V/Ti vs. radial distance trend) should be separately analyzed in each population. Only the lower V/Ti grains (towards the graphite exterior) have a convincing positive trend in V/Ti vs. grain size. In graphite e3, such an increase is consistent with the positive trends in both TiC size (Fig. 8) and the V/Ti ratio vs. radial distance in the graphite (Fig. 9). The TiC grains in this graphite apparently continued growing during graphite formation, simultaneously adding material that was more V-rich. The trend of increasing V/Ti with TiC size in e15 and e11 cannot be explained by this means, as neither graphite shows significant increases in TiC size with radial distance (Fig. 8).

It is useful here to consider the TiC nucleation and growth behavior. If the nucleation barrier is sufficiently large, with a corresponding large temperature range over which TiC nucleation occurs, then the V/Ti ratio in a particular TiC may reflect the temperature at which it nucleated. As the gas cools, the TiCs that nucleated first at higher temperatures will grow largest, while the Ti concentration in the gas is still high. TiCs nucleating later at lower temperatures will typically be smaller due to Ti depletion, and will also have a higher V/Ti ratio characteristic of this lower temperature. In such a case, a decrease in V/Ti vs. size would be expected, as small grains would have the highest V/Ti ratios (matching that in the gas) and large grains would have lower V/Ti ratios because they began their growth at higher temperatures. Since the observed trend in V/Ti vs. size is the opposite (larger TiCs have larger V/Ti), the V/Ti ratio does not reflect the temperature at which the TiC nucleated, but likely reflects its later growth behavior. Due to nucleation and initial growth at a higher temperature, all TiCs probably began with lower V/Ti ratios than they ultimately possessed. The observed V/Ti ratio increase with size might occur if only some of the grains continued growing at lower temperatures, simultaneously becoming more V-rich, while other grains had their growth arrested, keeping their lower V/Ti ratios. This would require preferential growth of only some grains, a size-dependent growth rate which would accelerate the growth of larger TiCs and cause them to develop higher V/Ti ratios than smaller grains. Such a size-dependent growth rate for TiCs could conceivably result from a dispersion in grain velocities, because larger grains would decelerate more slowly upon colliding with slower-moving pockets of gas. As noted above, TiC drift velocities of $\sim$100 km/s with respect to the gas are reasonable. At such velocities, TiC grains are moving far more quickly than Ti atoms at thermal speeds in the gas ($\sim$800 m/s at 1800°K), and the flux of Ti atoms on the

TiCs, and thus the TiC growth rate, becomes velocity-dependent. Grains that fluctuated to a slightly larger size would tend to maintain higher velocities against gas drag, and would grow more rapidly than smaller ones. These larger grains would then add more V-rich material during growth at lower temperatures and exhibit higher V/Ti ratios.

5. CONCLUSIONS AND PROSPECTS

Our isotopic and TEM study of SN graphites has shown them to be rich in internal grains, mostly TiCs and TiCs on which various iron–metal phases have condensed. Although these are relatively abundant for detection by microanalytical techniques (up to 2400 ppm of the graphite), the maximum concentrations are probably too low to be detected astronomically. The results of structural, chemical, and isotopic microanalyses presented here demonstrate that it is possible to arrive at a level of observational and interpretive detail that is entirely beyond the reach of traditional astronomical studies.

We anticipate that further studies of presolar grains from SN will open up new avenues for understanding the conditions of grain condensation in SN ejecta. For example, the phase assemblages and their compositions can be used to infer the condensation sequence, which in turn can guide future efforts in thermochemical modeling of grain condensation. In the present study, the observations indicate that TiCs were the first phase to condense and that their abundance relative to graphite decreased with time. The diversity of their properties (V/Ti atomic ratios, morphology, etc.) provides evidence that they had diverse formation histories and were subjected to different degrees of physical or chemical weathering before being trapped in the graphite. This evidence, in turn, implies some degree of turbulent mixing in the SN outflows. The TiC/Fe composite grains in some SN graphites, as well as solitary kamacites, give evidence that iron phases also condensed before graphite in many cases. This likely indicates considerable iron enrichment in the gas, but equilibrium thermochemical and chemical kinetic modeling is needed to determine from which SN shells (or mixtures of shells) the grains may have condensed, and how the condensation sequence may constrain the gas composition, temperature and pressure. Assuming that such modeling is feasible, it will be important to investigate further whether consistent condensation models can be constructed that take into account both the chemical and isotopic constraints provided by this and future microanalytical studies.

Some correlations among the various properties of the internal TiCs have been found, especially with regard to the chemical composition and the distance of a given internal grain from the graphite center (which is a rough measure of the time at which the grain was incorporated in the graphite). Detailed isotopic studies of these internal crystals and the graphite interiors with the NanoSIMS have yet to be performed, and it will be interesting to see if any isotopic trends are observed that mirror the chemical trends. In any event, the different chemical and physical trends seen among internal crystals indicate that the formation conditions of SN graphites are quite variable, so that it will be necessary to study many more SN graphites before a comprehensive understanding of their formation can emerge.

Acknowledgments—The authors wish to express profound thanks to Robert M. Walker for establishing the scholarly, congenial, inspirational and innovative scientific environment that made this study (as well as countless more like it) possible. We are indebted to Ramanath Cowsik for illuminating discussions. We also thank Larry Grossman, Rhonda Stroud, and an anonymous reviewer for constructive suggestions during the review process. This work was supported by NASA grants NAG5-10426 and NAG5-11865.

Associate editor: U. Ott

REFERENCES

Amari S., Lewis R. S., and Anders E. (1994) Interstellar grains in meteorites: I. Isolation of SiC, graphite, and diamond; size distributions of SiC and graphite. *Geochim. Cosmochim. Acta* **58,** 459–470.

Amari S., Zinner E., and Lewis R. S. (1995) Large ^{18}O excesses in circumstellar graphite grains from the Murchison meteorite: Indications of a massive-star origin. *Astrophys. J.* **447,** L147–150.

Amari S. and Zinner E. (1997) Supernova grains from meteorites. In *Astrophysical Implications of the Laboratory Study of Presolar Materials* (eds. T. J. Bernatowicz and E. Zinner), AIP Conf. Proc. **402,** pp. 287–305.

Anders E. and Grevesse N. (1989) Abundances of the elements: Meteoritic and solar. *Geochim. Cosmochim. Acta* **53,** 197–214.

Arendt R. G., Dwek E., and Moseley S. H. (1999) Newly synthesized elements and pristine dust in the Cassiopeia A supernova remnant. *Astrophys. J.* **521,** 234–245.

Bernatowicz T. J., Amari S., Zinner E. K., and Lewis R. S. (1991) Interstellar grains within interstellar grains. *Astrophys. J.* **373,** L73–76.

Bernatowicz T. J., Cowsik R., Gibbons P. C., Lodders K., Fegley B., Jr., Amari S., and Lewis R. S. (1996) Constraints on stellar grain formation from presolar graphite in the Murchison meteorite. *Astrophys. J.* **472,** 760–782.

Bernatowicz T. J. and Walker R. M. (1997) Ancient stardust in the laboratory. *Physics Today* **50,** 26–32.

Bernatowicz T. J. and Cowsik R. (1997) Conditions in stellar outflows inferred from laboratory studies of presolar grains. In *Astrophysical Implications of the Laboratory Study of Presolar Materials* (eds. T. J. Bernatowicz and E. Zinner), AIP Conf. Proc. **402,** pp. 451–474.

Bernatowicz T. J., and Zinner E. (1997) *Astrophysical Implications of the Laboratory Study of Presolar Materials. AIP Conf. Proc.* **402,** 750 pp.

Bernatowicz T., Amari S., Messenger S., and Lewis R. (1998) Internal structure and composition of presolar graphites from supernovae. *Lunar Planet. Sci. XXIX*. Lunar Planet. Inst., Houston. #1393 (abstr.).

Bernatowicz T., Bradley J., Amari S., Messenger S., and Lewis R. (1999) New kinds of massive star condensates in a presolar graphite from Murchison. *Lunar Planet. Sci. XXX*. Lunar Planet. Inst., Houston. #1392 (abstr.).

Buseck P. R. and Huang B. (1985) Conversion of carbonaceous material to graphite during metamorphism. *Geochim. Cosmochim. Acta* **49,** 2003–2016.

Chaudhuri D. K., Ravindran P. A., and Wert J. J. (1972) Comparative x-ray diffraction and electron microscopy study of the transformation-induced substructures in the iron-nickel martensites. *J. Appl. Phys.* **43,** 778–788.

Clayton D. D. (1975) ^{22}Na, Ne-E, extinct radioactive anomalies and unsupported ^{40}Ar. *Nature* **257,** 36–37.

Clayton D. D., Liu W., and Dalgarno A. (1999) Condensation of carbon in radioactive supernova gas. *Science* **283,** 1290–1292.

Cohen M. (1984) A study of extreme carbon stars. I - Silicon carbide emission features. *MNRAS* **206,** 137–147.

Croat T. K., Bernatowicz T., Stadermann F. J., Messenger S., and Amari S. (2002). Coordinated isotopic and TEM studies of a supernova graphite. *Lunar Planet. Sci. XXXIII.* Lunar Planet. Inst., Houston. #1315(abstr.).

Daulton T. L., Bernatowicz T. J., Lewis R. S., Messenger S., Stadermann F. J., and Amari S. (2002) Polytype distribution in circumstellar silicon carbide. *Science* **296,** 1852–1855.

Daulton T. L., Bernatowicz T. J., Lewis R. S., Messenger S., Stadermann F. J., and Amari S. (in press). Polytype distribution in circumstellar silicon carbide: Microstructural characterization by transmission electron microscopy. *Geochim. Cosmochim. Acta* **67**(24)**,** 4743–4767.

Gilra D. P. and Code A. D. (1971) The violet opacity in S, C-S and N stars and circumstellar silicon carbide grains. *Bulletin of the American Astronomical Society (BAAS)* **3,** 379 (abstr.).

Herant M. and Woosley S. E. (1994) Postexplosion hydrodynamics of supernovae in red supergiants. *Astrophys. J.* **425,** 814–828.

Hoppe P., Amari S., Zinner E., and Lewis R. S. (1995) Isotopic compositions of C, N, O, Mg, and Si, trace element abundances, and morphologies of single circumstellar graphite grains in four density fractions from the Murchison meteorite. *Geochim. Cosmochim. Acta* **59,** 4029–4056.

Keller L. P. and McKay D. S. (1997) The nature and origin of rims on lunar soil grains. *Geochim. Cosmochim. Acta* **61,** 2331–2341.

Lodders K. and Fegley B. Jr. (1995) The origin of circumstellar silicon carbide grains found in meteorites. *Meteoritics* **30,** 661–678.

Lodders K. and Fegley Jr. B. (1997) Condensation chemistry of carbon stars. In *Astrophysical Implications of the Laboratory Study of Presolar Materials* (eds. T. J. Bernatowicz and E. Zinner), AIP Conf. Proc. **402,** pp. 391–423.

McCray R. (1993) Supernova 1987A revisited. *Ann. Rev. A & A* **31,** 175–216.

Meikle W. P. S., Spyromilio J., Allen D. A., Varani G.-F., and Cummings R. J. (1993) Spectroscopy of supernova 1987A at 1–4 μm –II. Days 377 to 1114. *MNRAS* **261,** 535–572.

Merrill K. M. and Stein W. A. (1976) 2–14 μm stellar spectrophotometry. I. Stars of the conventional spectral sequence. *Publications of the Astronomical Society of the Pacific* **88,** 285–293.

Meyer B. S., Weaver T. A., and Woosley S. E. (1995) Isotope source table for a 25 M_O supernova. *Meteoritics* **30,** 325–334.

Roberts W., Rapp G., and Campbell T. (1990) Encyclopedia of Minerals 2nd ed. Van Nostrand Reinhold, New York.

Roche P. F., Aitken D. K., and Smith C. H. (1993) The evolution of the 8–13 micron spectrum of supernova 1987A. *MNRAS* **261,** 522–534.

Sharp C. M. and Wasserburg G. J. (1995) Molecular equilibria and condensation temperatures in carbon-rich gases. *Geochim. Cosmochim. Acta* **59,** 1633–1652.

Sheridan P. J. (1989) Determination of experimental and theoretical kASi factors for a 200-kV analytical electron microscope. *J. Electro. Microsc. Tech.* **11,** 41–61.

Stadermann F. J., Bernatowicz T., Croat T. K., Zinner E., Messenger S., and Amari S. (2003). Titanium and oxygen isotopic compositions of sub-micrometer TiC crystals within presolar graphite. *Lunar Planet. Sci. XXXIV.* Lunar Planet. Inst., Houston. #1627 (abstr.).

Travaglio C., Gallino R., Amari S., Zinner E., Woosley S., and Lewis R. S. (1999) Low-density graphite grains and mixing in type II supernovae. *Astrophys. J.* **510,** 325–354.

Treffers R. and Cohen M. (1974) High-resolution spectra of cool stars in the 10- and 20-micron regions. *Astrophys. J.* **188,** 545–552.

Upadhyaya G. S. (1996) *Nature and Properties of Refractory Carbides*. Nova Science, Commack, NY, pp. 126–127.

Ushakov A. I. and Litvintsev V. V. (1976) Relation between changes in the unit cell parameter and magnetic moment of iron-nickel alloys. *Phys. Met. Metal.* **42,** 182–183.

Williams D. B. and Carter C. B. (1996) *Transmission Electron Microscopy*. Plenum Press, New York. pp. 601–605.

Wooden D. H., Rank D. M., Bregman J. D., Witteborn F. C., Tielens A. G. G. M., Cohen M., Pinto P. A., and Axelrod T. S. (1993) Airborne spectrophotometry of SN 1987A from 1.7 to 12.6 microns—Time history of the dust continuum and line emission. *Astrophys. J. Suppl.* **88,** 477–507.

Wooden D. H. (1997) Observational evidence for mixing and dust condensation in core-collapse supernovae. In *Astrophysical Implications of the Laboratory Study of Presolar Materials* (eds. T. J. Bernatowicz and E. Zinner), AIP Conf. Proc. **402,** pp. 317–376.

Woolf N. J. (1973) Circumstellar infrared emission: Circumstellar origin of interstellar dust. In *Interstellar Dust and Related Topics* (eds. J. M. Greenberg and H. C. van de Hults), pp. 485–504. Int. Astro. Union Symp. 52. Reidel Publ., Dordrecht-Boston.

Woolf N. J. and Ney E. P. (1969) Circumstellar infrared emission from cool stars. *Astrophys. J. Lett.* **155,** L181–184.

Zinner E., Tang M., and Anders E. (1989) Interstellar SiC in the Murchison and Murray meteorites—Isotopic composition of Ne, Xe, Si, C, and N. *Geochim. Cosmochim. Acta* **53,** 3273–3290.

Zinner E. (1998) Stellar nucleosynthesis and the isotopic composition of presolar grains from primitive meteorites. *Ann. Rev. Earth Planet. Sci.* **26,** 147–188.